Electronic Supplementary Material (ESI) for Energy & Environmental Science.

Phase segregation of a composite air electrode unlocks the high performance of reversible protonic ceramic electrochemical cells

Fan He[1], Mingyang Hou[1], Dongliang Liu[2], Yong Ding[3], Kotaro Sasaki[4], YongMan Choi[5]*, Shihang Guo[6], Donglin Han[6], Ying Liu[7], Meilin Liu[3], and Yu Chen[1]*

[1]School of Environment and Energy, South China University of Technology, 382 East Road, Higher Education Mega Center, Guangzhou 510006, P. R. China.

[2]State Key Laboratory of Materials-Oriented Chemical Engineering, College of Chemical Engineering, Nanjing Tech University, Nanjing 210009, P. R. China.

[3]School of Material Science and Engineering, Georgia Institute of Technology, 771 Ferst Dr, NW, Atlanta, GA, 30309, USA

[4]Chemistry Division, Brookhaven National Laboratory, Upton, NY 11973, USA

[5]College of Photonics, National Yang Ming Chiao Tung University, Tainan 71150, Taiwan

[6]College of Energy, Soochow University, No 1 Shizi Street, Gusu District, Suzhou, 215006 China

[7]Research Institute of Renewable Energy and Advanced Materials, Zijin Mining Group Co., Ltd., Xiamen, Fujian 361101, China

*Corresponding authors. Email: YongMan Choi (ymchoi@nycu.edu.tw); Yu Chen (eschenyu@scut.edu.cn)

Experimental section

Materials synthesis: The $Ce_{0.2}Ba_{0.2}Sr_{0.2}La_{0.2}Ca_{0.2}CoO_{3-\delta}$ (CBSLCC) composite (hereafter, CBSLCC refers to the three-phase composite) was synthesized by a sol-gel complexing method.[1] According to the nominal composition of the CBSLCC material, stoichiometric numbers of $Pr(NO_3)_3 \cdot 6H_2O$, $Ba(NO_3)_2$, $Sr(NO_3)_2$, $Ca(NO_3)_2$, $La(NO_3)_3$, $Co(NO_3)_2 \cdot 6H_2O$ were mixed with complexing agents of EDTA and citric acid in deionized water. $NH_3 \cdot H_2O$ was then added to adjust the pH of the solution to 7. A gel was formed with continuous stirring and heating at 90 °C. Subsequently, the obtained gel was dried at 300 °C for 5 h in an oven for precursors. Finally, the precursors were calcined at 950 °C for 10 h to obtain CBSLCC powders. $PrBaCo_2O_{5+\delta}$ (PBC), $Ba_{0.5}Sr_{0.5}Co_{0.8}Fe_{0.2}O_{3-\delta}$ (BSCF), $BaCo_{0.4}Fe_{0.4}Zr_{0.1}Y_{0.1}O_{3-\delta}$ (BCFZY), $Ce_{0.052}Ba_{0.242}Sr_{0.232}La_{0.232}Ca_{0.242}CoO_{3-\delta}$ (Syn-CD-CBSLCC) (We denote the intentionally synthesized CD-CBSLCC as Syn-CD-CBSLCC), $La_{0.5}Sr_{0.5}CoO_{3-\delta}$ (LSC), and $PrBa_{0.5}Sr_{0.5}Co_{1.5}Fe_{0.5}O_{5+\delta}$ (PBSCF) samples were prepared by the same method, calcined at 1000, 950, 1000, and 950 °C for 5 h, respectively. $BaZr_{0.1}Ce_{0.7}Y_{0.1}Yb_{0.1}O_{3-\delta}$ (BZCYYb) electrolyte material was synthesized by a solid-state reaction method. ZrO_2, $BaCO_3$, CeO_2, Y_2O_3, and Yb_2O_3 as raw materials were mixed by ball milling for 12 h, and then calcined at 1250 °C for 10 h to obtain final powders.

Cell preparation: BZCYYb-electrolyte-supported symmetrical cells were prepared for electrochemical impedance spectroscopic (EIS) measurements. The BZCYYb powders were dry-pressed into pellets with a diameter of 13.0 mm and calcined at 1450 °C for 5 h to obtain dense pellets. Subsequently, the cathode suspension, composed of the cathode materials, ethyl cellulose, and terpineol at a weight ratio of 1:0.04:0.76, was printed on two sides of BZCYYb pellets, and then calcined at 950 °C for 2 h. The silver ink was covered on the surface of the electrode for EIS tests. Ni-BZCYYb anode-supported half-cells were fabricated by dip-coating and co-sintering. An anode slurry was obtained by the ball-milling of NiO and BZCYYb powders, polyethersulfone (PESf), polyvinyl pyrrolidone (PVP), and N-Methyl pyrrolidone (NMP) for 24 h. After the phase inversion processes recently reported,[2] the raw tube was heated to 1000 °C to obtain the anode substrate. Ni-

BZCYYb functional layer and electrolyte were then dip-coated onto the green tube substrate. The half-cell tube was co-sintered at 1450 °C for 5 h. The air electrode slurry was printed onto the electrolyte surface of the half-cell, and then co-fired at 950 °C for 2 h to obtain the single cell. The effective area of single cells was 0.21 cm^{-2}. The silver wires were used as current collectors.

Characterization and electrochemical tests: Fourier transform infrared (FTIR) spectroscopic measurements were performed using a Bruker Vertex 70 Hyperion 1000. Water content was determined by Karl-Fischer titration method. The samples were dry-pressed into pellets and then sintered at 1050°C for 10 h, and then hydrated by annealing at the desired temperature in wet air. The water contained in the samples was evaporated by an ADP-512S furnace (Kyoto Electronics Manufacturing Co., Ltd, Kyoto, Japan) kept at 1000 °C and was carried by dry N_2 flow (200 mL min^{-1}) into an MKC-710S titration cell (relative standard deviation ≤ 0.3%). Raman spectroscopy (RenishawRM1000) was applied with a wavelength of 514 nm. All X-ray absorption spectroscopy (XAS) data was analyzed following the standard procedures in the program Demeter.[3] The $k^2\chi(k)$ functions were then Fourier transformed into R-space, with the Hanning-type window in the range of 2-10 Å. Least-squares curve parameter fitting was performed to obtain the quantitative structural parameters around the Ce cations. To evaluate the electrochemical performance of symmetrical cells, EIS was conducted in a tube furnace with temperature and atmosphere control. Input gas humidity was controlled by adjusting the scrubbing bottle temperature at a rate of 60 mL min^{-1}. EIS spectra were measured using an electrochemical workstation (AMETEK PARSTAT MC). For fuel-cell tests, the fuel electrode was flowed with hydrogen at a rate of 60 mL min^{-1}, while the air electrode was exposed to ambient air. For electrolysis-cell tests, the fuel electrode was flowed with hydrogen at a rate of 60 mL min^{-1}, while the air electrode was exposed to wet air (3% H_2O) at a rate of 60 mL min^{-1}. For Faradaic efficiency tests, the hydrogen fuel at the fuel electrode was replaced by 10% hydrogen/argon to ensure hydrogen production at a rate of 60 mL min^{-1}, and the air electrode was provided by humidified air (3%, 30%, 50%, and 60% H_2O) at a rate of 60 mL min^{-1}. For the reversible stability tests, the cell was discharged at ±0.5 A cm^{-2}

when the air electrode was exposed to wet air (30% H_2O) at a rate of 60 mL min^{-1}, and the fuel electrode was fueled by hydrogen at a rate of 60 mL min^{-1}. The frequency range for all impedance measurements was between 100 mHz and 10 kHz with an AC amplitude of 10 mV.

Computational methods: Density functional theory (DFT) calculations were conducted using the Vienna ab initio simulation package (VASP)[4, 5] with the PBE generalized gradient approximation (GGA)[6] and the projector-augmented wave (PAW) method.[7] A plane-wave basis set with a cut-off energy of 415 eV was used, and the spin-polarization method was applied. Ce, Ba_sv, Sr_sv, La, Ca_sv, Co, and O_s (soft O potential) of PAW_PBE were applied in this study.

The bulk structures of $(Ce_{0.1875}Ba_{0.1875}Sr_{0.1875}La_{0.1875}Ca_{0.1875})CoO_3$ (CBSLCC, $Pm\bar{3}m$) and CeO_2 ($Fm\bar{3}m$) were optimized with the Hubbard U correction (PBE + U) with $U_{eff,\ Ce}$ = 5.0 eV[8] and $U_{eff,\ Co}$ = 4.0 eV[9] (**Fig. S30**). Then, the additional Ce-deficiency effect was examined by removing one Ce in CBSLCC (CD-CBSLCC, $(Ce_{0.125}Ba_{0.1875}Sr_{0.1875}La_{0.1875}Ca_{0.1875})CoO_3$). Also, the Ce deficiency was implemented by removing the Ce atom from the CeLaCaO layer (**Fig. S30b**) after optimization calculations. The first Brillouin zone (BZ) of the unit cell was sampled with a (3 × 3 × 3) or (4 × 4 × 4) ***k***-point grid for bulk models of CeO_2 and CBSLCC, respectively. The density of states (DOS) for bulk CBSLCC and CD-CBSLCC was calculated using PBE + U with the Gaussian smearing method of σ = 0.2 eV and the Γ-centered (3 × 3 × 3) ***k***-point mesh. The O 2*p*-band center[10, 11] was calculated only with occupied states by integrating from their negative infinity to the Fermi energy at 0 eV). In particular, the corrected total energy of O_2 ($E(O_{2,corr})$) was applied after correction using the experimental binding energy of oxygen (5.12 eV),[12] as reported.[13] 2D slab models of O-terminated six-trilayer CeO_2(111) with one oxygen vacancy on the top layer and Ce-deficient eight-layer CoO-terminated CBSLCC(001) with six oxygen vacancies, including one on the top layaer, were constructed for mechanistic studies. Half of the layers were fixed at the bulk parameters for optimization with the Γ-centered (3 × 3 × 1) ***k***-point grid, while dipole correction and a vacuum space of 15 Å were applied.

Adsorption energies (ΔE_{ads}) on the most stable CoO-terminated (001) surface of CBSLCC(001)[14] and $CeO_2(111)$[8, 15] were calculated by ΔE_{ads} = E(surf-ads) – (E(surf) + $E(O_{2,corr})$), where E(surf-ads) and E(surf) are the DFT energies of an adsorbate on a bare surface and a clean surface, respectively. The cohesive energy[16] that is a descriptor in examining the phase stability was calculated to investigate that of $(Ce_{0.1875}Ba_{0.1875}Sr_{0.1875}La_{0.1875}Ca_{0.1875})CoO_3$ (CBSLCC) and a Ce-deficient CBSLCC ($(Ce_{0.125}Ba_{0.1875}Sr_{0.1875}La_{0.1875}Ca_{0.1875})CoO_{3,}$ hereafter referred to as CD-CBSLCC) (**Tables S8** and **S9**). The cohesive energy of bulk CBSLCC and CD-CBSLCC (eV/atom) is defined and calculated with $4 \times 4 \times 4$ **k**-point mesh. E_{coh} = ((E(total) – n×E(atom))/n, where E_{coh} is the cohesive energy per atom, E(total) is the DFT energy of a bulk structure, E(atom) is the DFT energy of a gas-phase atom, and n is the number of atoms in the bulk structure. The surface energies (E_{surf}) in J/m^2 were first calculated to investigate the surface stabilities[17] by $E_{surf} = (E_{slab} - E_{bulk})/2A$, where E_{slab} and E_{bulk} are the DFT energies of surfaces and bulk structures, respectively (**Table S9**). The mechanistic study on reversible oxygen reduction and oxygen evolution was examined using the adsorption energies calculated on CBSLCC(001) and $CeO_2(111)$ and the climbing-image nudged elastic band method (CI-NEB).[18]

Supplementary Note 1

Oxygen exchange kinetics of the CBSLCC electrode evaluated by EIS and DRT

To investigate the oxygen exchange kinetics (highly associated with oxygen reduction reaction) of the CBSLCC electrode, the EIS measurements under different oxygen partial pressures (pO_2) were conducted at 600 °C (**Fig. S13a**). When exposed to the air containing different p_{O2} from 0.1 to 1.0 atm at 600 °C, the ASRs of the CBSLCC electrode continuously decreased from 0.41 to 0.19 Ω cm^2. The specific rate-limiting during the oxygen exchange process can be ascertained by the R_p variations at different $p(O_2)$, expressed as $R_p \propto p(O_2)^{-n}$.[19, 20] The n value of the CBSLCC is fitting to be 0.23 (**Fig. S13b**). When n = 0.25, $O_{ads} + 2e^- + V_{O(s)}^{\bullet\bullet} \leftrightarrow O_{O(s)}^{\bullet}$ is considered the rate-determining step.[21, 22] We also utilized the distribution of relaxation time (DRT) tool to simplify the entire complex electrode reaction into several key isolated reactions (**Fig. S13c**, DRT codes were from Prof. Ciucci's group).[23] Briefly, each curve at different pO_2 was separated into three peaks of high frequency (HF), intermediate frequency (IF), and low frequency (LF). Based on the frequency range, the electrode reaction process can be deconvoluted into three independent electrochemical processes. The general dependence of R_p on pO_2 can be approximated by the equation $R_p = k(pO_2)^{-n}$. According to the fitting equation of $R_p = k(pO_2)^{-n}$ (**Fig. S13d**), n = 0.34 for the peaks at LF suggests that the process may be related to oxygen ion incorporation and charge transfer across the interface.[21, 22] Similarly, n = 0.33 for the peaks at IF indicates that the IF process is also likely associated with oxygen ion incorporation and charge transfer across the interface.[21, 22] The changes in pO_2 were relatively insensitive for the peaks at HF (n = 0.12), suggesting that HF peaks were likely related to the second charge transfer of O^- to O^{2-}.[24, 25]

Supplementary Note 2

Surface exchange coefficient (k^*_{chem}) and bulk diffusion coefficient (D^*_{chem}) of CBSLCC

The surface exchange coefficient (k^*_{chem}) and bulk diffusion coefficient (D^*_{chem})

of CBSLCC were determined by the electrical conductivity relaxation (ECR) method at 500-650 °C. Before ECR measurements, 0.8 g CBSLCC powder was dry-pressed and then calcined at 1150 °C for 10 h to obtain a dense bar sample (7.84 mm × 4.43 mm × 1.66 mm). By suddenly switching the oxygen partial pressure from 0.21 to 0.1 atm, the conductivity of the material tends to a new balance to induce a relaxation of conductivity, and detected by the DC 4 probe. The D^*_{chem} and k^*_{chem} can be calculated by a simulation of the conductivity relaxation curve, as shown in **Fig. S14a**. Compared with the highly active air electrode materials reported recently, the CBSLCC has outstanding D^*_{chem} and k^*_{chem} at intermediate temperatures of 500-700 °C (**Fig. S14b**).[26-29] For instance, k^*_{chem} of CBSLCC is 2.15×10^{-4} cm s^{-1} at 550 °C, surpassing the excellent $Ba_{0.5}Sr_{0.5}Co_{0.8}Fe_{0.2}O_{3-\delta}$ (BSCF) (1.2×10^{-4} cm s^{-1}) and $BaCo_{0.4}Fe_{0.4}Zr_{0.1}Y_{0.1}O_{3-\delta}$ (BCFZY) (1.9×10^{-4} cm s^{-1}) electrodes under the same conditions.[28]

Supplementary Note 3

The hydration reaction kinetics of the CBSLCC electrode evaluated by EIS and DRT

Shown in **Fig. S15a** (inset) is the impedance spectra of the CBSLCC electrode tested at 600 °C under various conditions of air containing different pH_2O. When the humidified air was swept into the electrode chamber, the complexity of the symmetrical cell system may be largely increased, and the oxygen partial pressure (pO_2) and water partial pressure (pH_2O) are changed. The typical hydration reaction ($H_2O + V_O^{\bullet\bullet} + O_O^{\times} \leftrightarrow 2OH_O^{\bullet}$) can be described as follows. Specifically, oxygen vacancies are first occupied with reduced oxygen species ($\frac{1}{2}O_2 + V_O^{\bullet\bullet} \leftrightarrow 2O_O^{\times} + 2h^{\bullet}$),[30] and uptake of the hydrated proton ($OH_O^{\bullet}$) is introduced into the electrochemical process via the expense of the formed electron holes ($H_2O + 2O_O^{\times} + 2h^{\bullet} \leftrightarrow 2OH_O^{\bullet} + \frac{1}{2}O_2$).[31] Such a hydration reaction has a significant

impact on the surface electrode reaction and bulk ion diffusion. Similarly, we utilized DRT analysis to deconvolute the EIS of the symmetrical cell with the CBSLCC electrode as a function of pH_2O at 600 °C (**Fig. S15a**). As fitting from the equation of $R_p = k(pH_2O)^{-m}$, the reaction order of m value is considered to simplify the electrode reaction in regard to pH_2O. As shown in **Figure S15b**, m = 0.04 and m = 0.12 at HF and IF ranges indicated that the electrochemical processes at HF and IF ranges have little dependence on the variation of pH_2O. However, the R_p at the LF range were sensitive to the changes in $p(H_2O)$, as signified by m = 0.92. m = 0.92 at the LF range was more likely associated with the electrode processes of the surface water formation ($H^+_{TPB} + OH^-_{TPB} \rightarrow H_2O_{TPB}$) or/and water desorption from the electrode surface ($H_2O_{TPB} \rightarrow H_2O_{(gas)}$).[21, 22]

Supplementary Note 4

DRT analysis of the cells with the CBSLCC electrodes before and after the introduction of steam (3% H_2O) into air

Shown in **Fig. 2b** are EIS of the cells with the CBSLCC electrodes at 500 °C before and after the introduction of steam (3% H_2O) into air. For instance, area-specific resistances (ASRs) of the cell with CBSLCC electrode are 1.65 Ω cm^2 and 0.09 Ω cm^2 in wet air (3% H_2O) at 500 °C and 650 °C, much lower than those (2.43 Ω cm^2 at 500 °C and 0.13 Ω cm^2 at 650 °C) in dry air. To verify the contribution of self-assembled CBSLCC for the electrochemical reactions, we implemented the DRT analysis on the corresponding EIS in dry and wet air, as shown in **Fig. S17**. It is comparatively found that the decrease of R_p concentrated on the peak at intermediate and low-frequency ranges. Based on the aforementioned DRT analysis (**Fig. S13** and **S15**), two optimized electrode processes at IF and LF are the processes of oxygen ion incorporation with the charge transfer and the water formation and desorption from the electrode surface, respectively.[21, 22] This may be attributed to the self-assembled CeO_2 phase and highly active CD-CBSLCC in the CBSLCC composite, as demonstrated in **Fig. 2g** and **Fig. 4**.

Supplementary Note 5

Design and demonstration of CeO_2 for the enhancement on the ionic conductivity and hydration

To identify the role of CeO_2 for the drive to the ionic conduction and hydration, we carried out controlled experiments to consider its impacts on the electrochemical performance (**Fig. S20**). The triple-conducting $PrBa_{0.5}Sr_{0.5}Co_{1.5}Fe_{0.5}O_{5+\delta}$ (PBSCF) was chosen as a parent electrode material. We further uniformly mixed 15 wt% CeO_2 oxide into the 85 wt% PBSCF powder as a simulated self-assembled composite using a high-energy balling mill. PBSCF is an archetypal air electrode extensively intended for application in protonic ceramic fuel cells (PCFCs), exhibiting remarkably electrocatalytic activity with exceptional phase compatibility and robustness.[32] The mixed composite of 15 wt% CeO_2 and 85 wt% PBSCF exhibited a lower R_p of 0.13 Ω cm^2 compared to the original PBSCF (0.16 Ω cm^2) at 650 °C in dry air (**Fig. S21a**, top). The decreasing R_p is likely ascribed to the impressive oxygen ionic conductivity of CeO_2 in the mixed composite of 15 wt% CeO_2 and 85 wt% PBSCF. In term of the hydration of CeO_2, we compared the EIS of the mixed composite (Its composition is 15 wt% CeO_2 and 85 wt% PBSCF) in wet air with those of the original PBSCF in dry and wet air at 550 °C (**Fig. S21a**, bottom). When mixed with 15 wt% CeO_2, the PBSCF exhibited the lowest R_p of 0.94 Ω cm^2 in wet air at 550 °C, suggesting the hydration capability of triple-conducting PBSCF is strengthened due to the contribution of CeO_2. To further verify the contributions from each process, the DRT analysis of EIS was performed (**Fig. S21b**). Clearly, similar decreases on the R_p of processes at IF and LF are also found in the DRT of the mixed composite of 15 wt% CeO_2 and 85 wt% PBSCF. Such enhancement on the processes of ionic transfer and gas diffusion is consistent with the DRT analysis on the EIS of the CBSLCC electrode in dry and wet air, strongly demonstrating that the role of the CeO_2 phase can accelerate the rate of oxygen ion incorporation and enhance the water formation/desorption process.

Supplementary Note 6

Hydration behavior of the CBSLCC evaluated by XPS technology

To reveal the high-entropy surface for the process of the hydration reaction, we carried out several spectroscopic measurements of X-ray photoelectron spectroscopy (XPS) to determine the variation in surface properties of the CBSLCC powders before and after the steam-treatments in wet air (30% H_2O) at 650 °C for 50 h (**Fig. S22**). It is clearly found that the ratio of the surface H_2O species (H_2O_{ads}) was largely increased from 23.97% to 38.64% after being interacted in wet air (30% H_2O) at 650 °C for 50 h. The H_2O adsorption capacity of the CBSLCC powder can be partially verified by the O 1s XPS fitting curves, which is considered a vital prerequisite for the hydration reaction. The consumption of lattice oxygen species ($O_{Lattice}$, $O_O^{\times}$) on the steam-treated CBSLCC may be ascribed to the occurrence of hydration reaction ($H_2O + V_O^{\bullet\bullet} + O_O^{\times} \leftrightarrow 2OH_O^{\bullet}$) when exposed to a humidified air (30% H_2O) atmosphere. And a corresponding decrease in the oxygen vacancy concentration ($V_O^{\bullet\bullet}$) of steam-treated CBSLCC led to a less amount of the adsorbed oxygen species (O_{ads}, OH^-/O_2).

Supplementary Note 7

Hydrated proton desorption temperature of CBSLCC, analyzed from TGA curves

To verify the binding energy of hydrated proton ($OH_O^{\bullet}$) with the CBSLCC composite, we implemented sets of TGA experiments of the CBSLCC and PBC powders before and after the treatments in wet air (30% H_2O) at 650 °C for 50 h (**Fig. 2e, 2f and S23**). The surface adsorbed species (steam and gas) of the powder were fully desorbed by the thermostatic process at 100 °C for half an hour using the flowing air of 20 ml min^{-1}. Thus, the weight loss of the CBSLCC and PBC powders without the steam treatments is ascribed to the desorption of oxygen from the lattice at the elevated temperatures of 100-800 °C. When being interacted in wet air (30% H_2O) at 650 °C for 50 h, the weight loss of the steam-treated CBSLCC and PBC samples is composed of the desorption of oxygen and water (H_2O). Then, we calculated the weight loss from the desorption of H_2O (dehydration), as shown in **Fig. 2f**. Specifically, the main H_2O

desorption peaks of the PBC sample are located at 600 °C. While the main H_2O desorption peak (at 800 °C) of CBSLCC composite is much higher than that of PBC, which is contributed to the stronger binding energy of CBSLCC composite with hydrated protons. Such enhanced hydration strength may be due to the role of the self-assemble CeO_2 secondary phase in the CBLSCC composite, which can be also found in **Fig. 2g**.

Supplementary Note 8

Adsorbed H_2O and proton uptake capabilities of the steam-treated CBSLCC evaluated by the Fourier transform infrared spectroscopy (FTIR) measurement

According to the typical Kroger¨-Vink expression (hydration reaction) given as $H_2O(gas) + V_O^{\bullet\bullet} + O_O \rightarrow 2OH_O^{\bullet}$,[33] when exposed to the steam, the hydration reaction occurred at the gas-solid interface could generate abundant $OH_O^{\bullet}$. The signature of $OH_O^{\bullet}$ and H_2O can be both detected by the Fourier transform infrared spectroscopy (FTIR) measurement, reflected as a broad peak at a range of 3300-3700 cm^{-1}.[34, 35] The powder samples were pre-treated in wet air (50% H_2O) at 600 °C for 50 h, and quenched at 300 °C in air for the full desorption of H_2O on the powder surface. The pellets for the FTIR measurements were fabricated by uniformly mixing the KBr (analytical purity, Sinopharm Chemical Reagent Co., Ltd.) under the infrared lamp. The negative OH peak intensity of the steam-treated CBSLCC was more pronounced than that of the steam-treated PBC, slightly higher than that of the steam-treated CeO_2 (**Fig. 2g**). Such higher OH peak intensity of the steam-treated CBSLCC was due to the contributions of the CeO_2 phase on the adsorbed H_2O capability and main $Ce_{0.2-y}Ba_{0.2}Sr_{0.2-x}La_{0.2-x}Ca_{0.2}CoO_{3-\delta}$ perovskite phase on the more formed hydrated protons (enhanced OER activity).

Supplementary Note 9

Advantages of the tubular single cells fabricated via the phase inversion process

Shown in **Fig. S25** are SEM images of different sections of the tubular cell after

the electrochemical tests. The thickness of the fabricated tubular cell was around 500 μm with abundant straight finger-like pores (**Fig. S25a**). Straight finger-like pores with size of 30-100 μm in length can be found between the anode supporting layer and electrolyte (**Fig. S25b**). Such porous fuel electrodes with a high surface area can accelerate the mass and gas transport during the electrocatalysis process. The unique characteristics of microstructures are critical to enhancing the performance and stability of the cell under realistic operation conditions.[2] Our fabricated tubular cell was composed of a porous fuel-electrode-supported layer (FSL), a fine fuel-electrode functional layer (FFL), a dense BZCYYb electrolyte (≈6 μm), and the high-entropy self-assemble CBSLCC air electrode (with the active area of 0.21 cm^{-2}), respectively (**Fig. S25c**). The BZCYYb material has been applied as the electrolyte and ceramic phase in anode due to its relatively high ionic conductivity at reduced temperatures.[36] The CBSLCC air electrode demonstrated a rough active surface with considerable decorates of nanoparticles, providing more active sites for ORR and OER (**Fig. S25d**).

Supplementary Note 10

Performance comparisons in fuel cell mode

To better show the comparison of fuel-cell performances, the performances of different material systems (electrolyte and operation conditions) were summarized in **Supplementary Table 6**.[27, 28, 34, 37-48] For instance, Saqib et al. has reported that a PCEC with the misfit-layered $Gd_{0.3}Ca_{2.7}Co_{3.82}Cu_{0.18}O_{9-\delta}$ (GCCCO) air electrode showed the maximum powder densities of 1.16 and 2.05 W cm^{-2} at 600 and 700 °C, respectively.[47] With the novel concept of revitalizing interface by an acid etch, the fabricated PCEC achieved exceptional performance down to 350 °C, with peak power densities of 1.6 W cm^{-2} at 600 °C, and 0.65 W cm^{-2} at 450 °C when the feedstocks are pure H_2 for the fuel electrode and 70% O_2-30% H_2O for the air electrode.[37] The $Ba_{0.9}Co_{0.7}Fe_{0.2}Nb_{0.1}O_{3-\delta}$ (BCFN) electrode with a water-promoted surface restructuring process has been recently proposed for the application of PCEC.[46] Excellent performance was demonstrated with a P_{max} of 1.70 W cm^{-2} at 650 °C. The A-site high-entropy engineer has been currently utilized to optimize the catalytic activity and durability of the air

electrode. For example, a PCEC with the $Pr_{0.2}Ba_{0.2}Sr_{0.2}La_{0.2}Ca_{0.2}CoO_{3-\delta}$ (PBSLCC) electrode demonstrated a high P_{max} of 1.52 W cm^{-2} at 650 °C.[27] Therefore, for self-assembled CBSLCC electrode enabled PCEC in this work, the achieved cell performances of 2.15 W cm^{-2} at 650 °C and 1.66 W cm^{-2} at 600 °C, have surpassed these advanced high-performance air electrodes, which have been recently developed.

Supplementary Note 11

Faradaic efficiency on Ni-BZCYYb anode-supported tubular PCEC at different operating conditions.

Faradaic efficiency could be defined as the efficiency with which electrons participate in the desired reaction in an electrochemical system. The actual amount of H_2 produced by the electrolysis cell was collected and detected by on-line GC equipment, and the Faradaic efficiency can be simply described as the ratio of the actual amount of H_2 to the predicted amount of H_2 from the current passing through the cell using Faraday's law of electrochemical equivalence.[49] It is apparently found that the Faradaic efficiency was impacted by the operating temperature and steam concentration (**Fig. S27**). When the cell was applied at different current densities of -0.5, -0.75, and -1.0 A cm^{-2} under the humidified air (50% H_2O) atmosphere, the voltages increased from 1.13 to 1.19 and 1.24 V, respectively (**Fig. S27a**). The corresponding Faradaic efficiency dropped from 90.3% to 87.3% and 83.0% with an increase in the cell voltages from 1.13 to 1.19 and 1.24 V, respectively (**Fig. S27a**). Furthermore, the effects of steam concentration on the Faradaic efficiency were investigated at a fixed current density of -1 A cm^{-2} at 600 °C. As illustrated in **Fig. S27b**, it appears that Faradaic efficiencies obviously increased from 81.8% to 82.2%, 87.3%, and 91.1% with the higher steam concentrations of 3%, 30%, 50%, and 60%, respectively. The corresponding H_2 production rates at different electrolysis voltages and various H_2O concentrations are also shown in **Fig. S28**.

Supplementary figures and tables

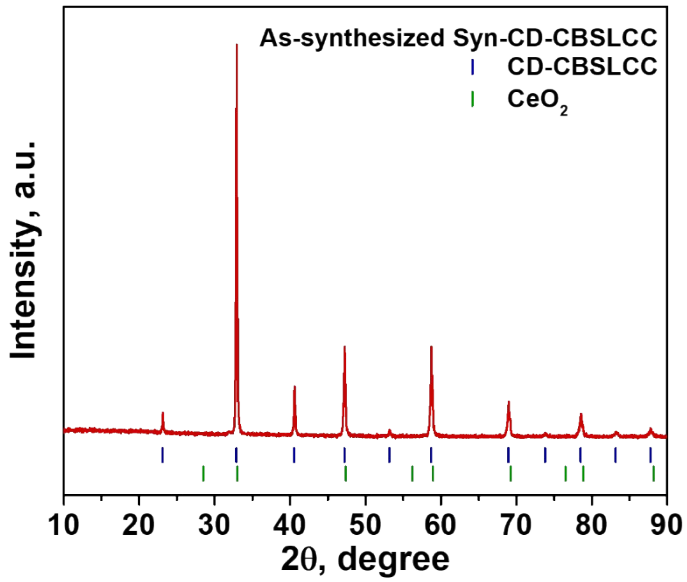

Fig. S1. XRD patterns of the Syn-CD-CBSLCC sample sintered at 950 °C for 5 h.

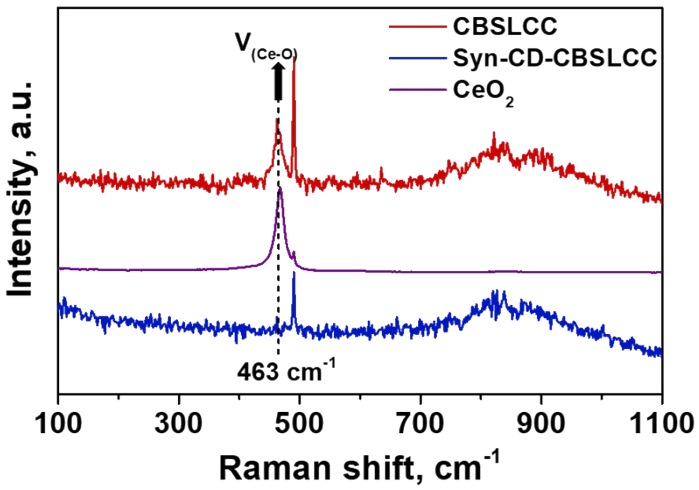

Fig. S2. Raman spectra of CBSLCC, CeO_2 and Syn-CD-CBSLCC.

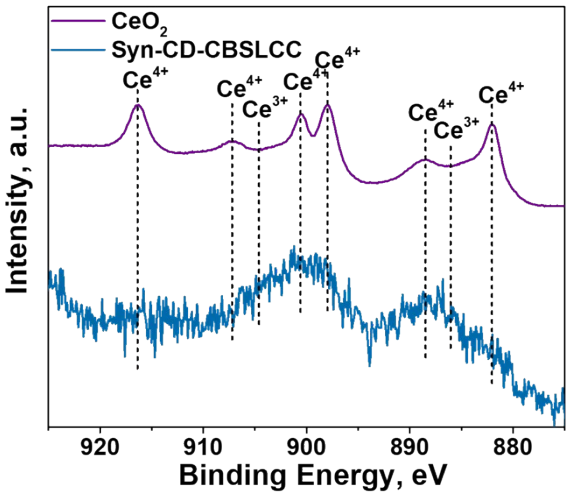

Fig. S3. Ce 3d XPS curves of the CeO_2 and Syn-CD-CBSLCC samples.

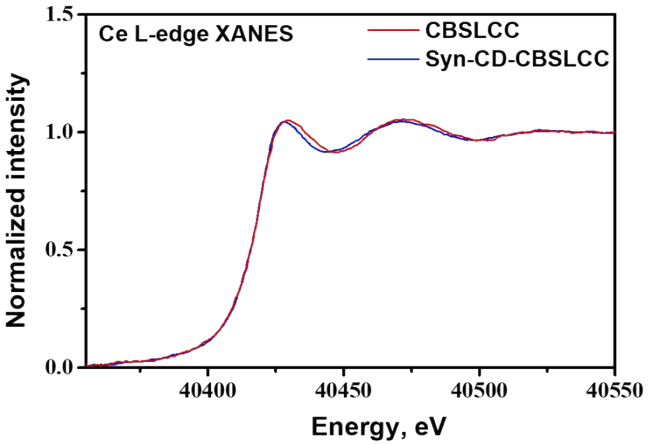

Fig. S4. The spectra of Ce L-edge X-ray absorption near edge structure (XANES) for the CBSLCC and Syn-CD-CBSLCC samples.

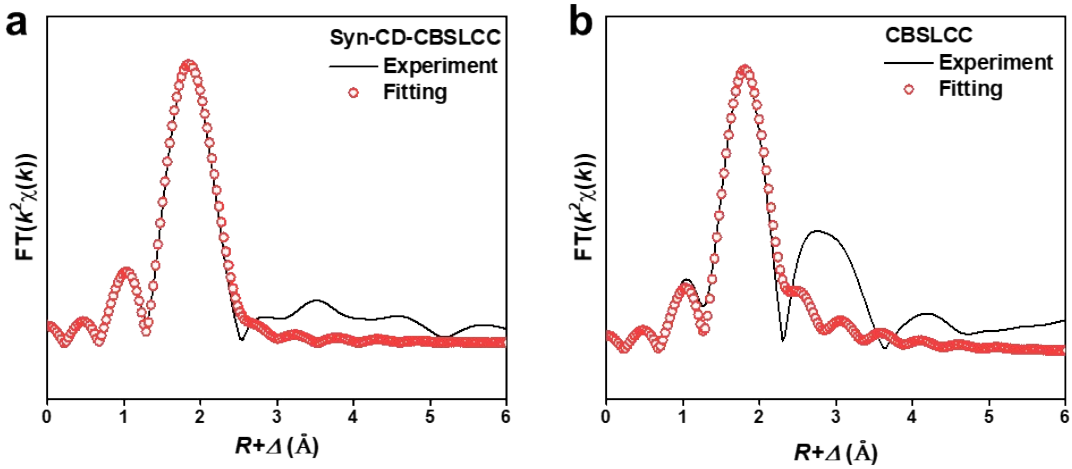

Fig. S5. Fourier-transformed extended X-ray absorption fine structure (EXAFS) data measured at the Ce L-edge and its fitting curve for **(a)** Syn-CD-CBSLCC and **(b)** CBSLCC samples.

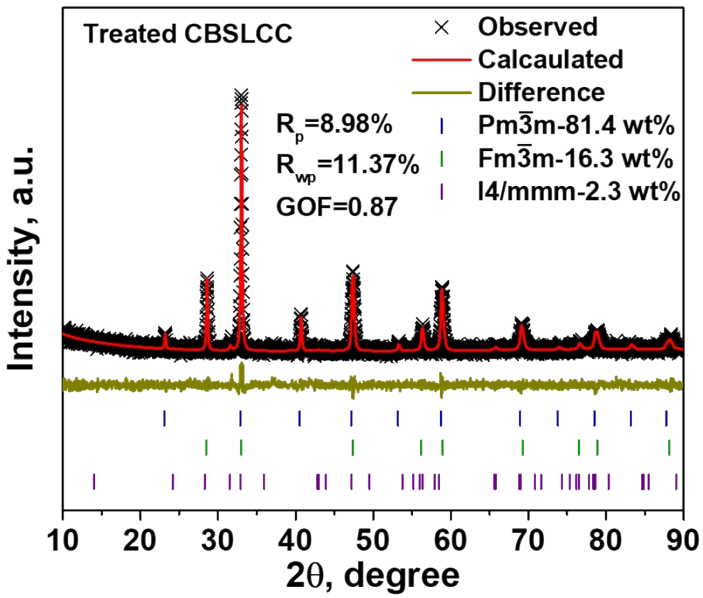

Fig. S6. A Rietveld XRD refinement of the CBSLCC powder after interacting at 650 °C in wet air (30% H_2O, 50 h).

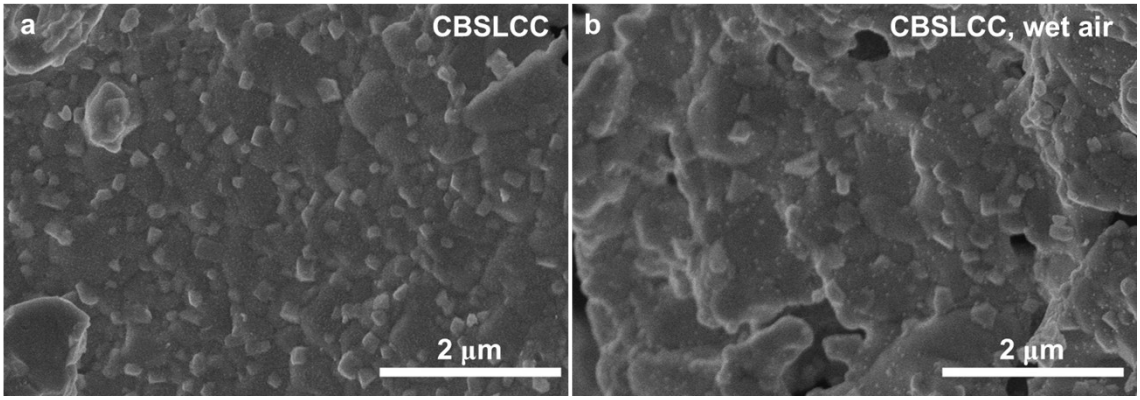

Fig. S7. SEM images of CBSLCC powders **(a)** and after treatments in wet air (30% H_2O) at 650 °C for 50 h **(b)**.

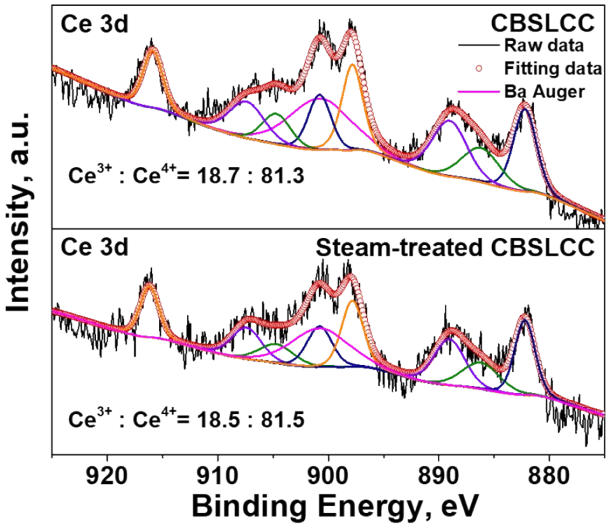

Fig. S8. Fitted Ce 3d XPS curves of the CBSLCC samples before and after treatment in wet air (30% H_2O) at 650 °C for 50 h.

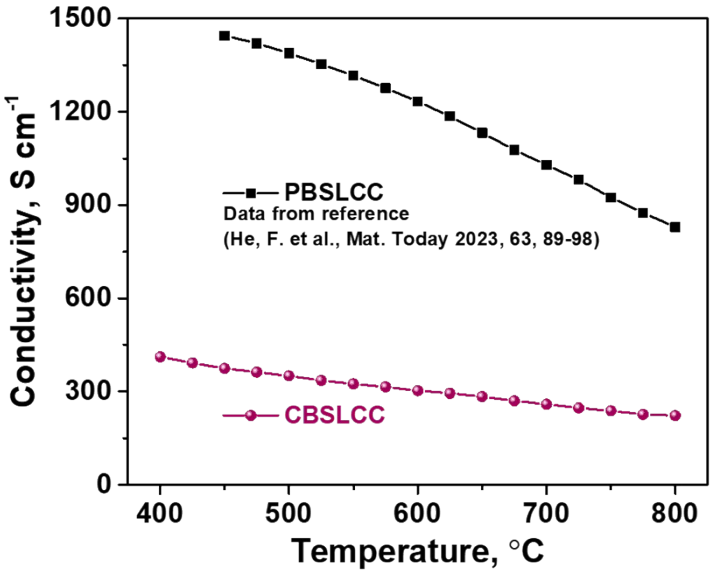

Fig. S9. Electrical conductivities of CBSLCC sample at 400-850 °C in air in comparison with those of high-entropy PBSLCC reported recently (Reference[50]: He, F. *et al.* A reversible perovskite air electrode for active and durable oxygen reduction and evolution reactions via the A-site entropy engineering. *Materials Today* **63**, 89-98 (2023)).

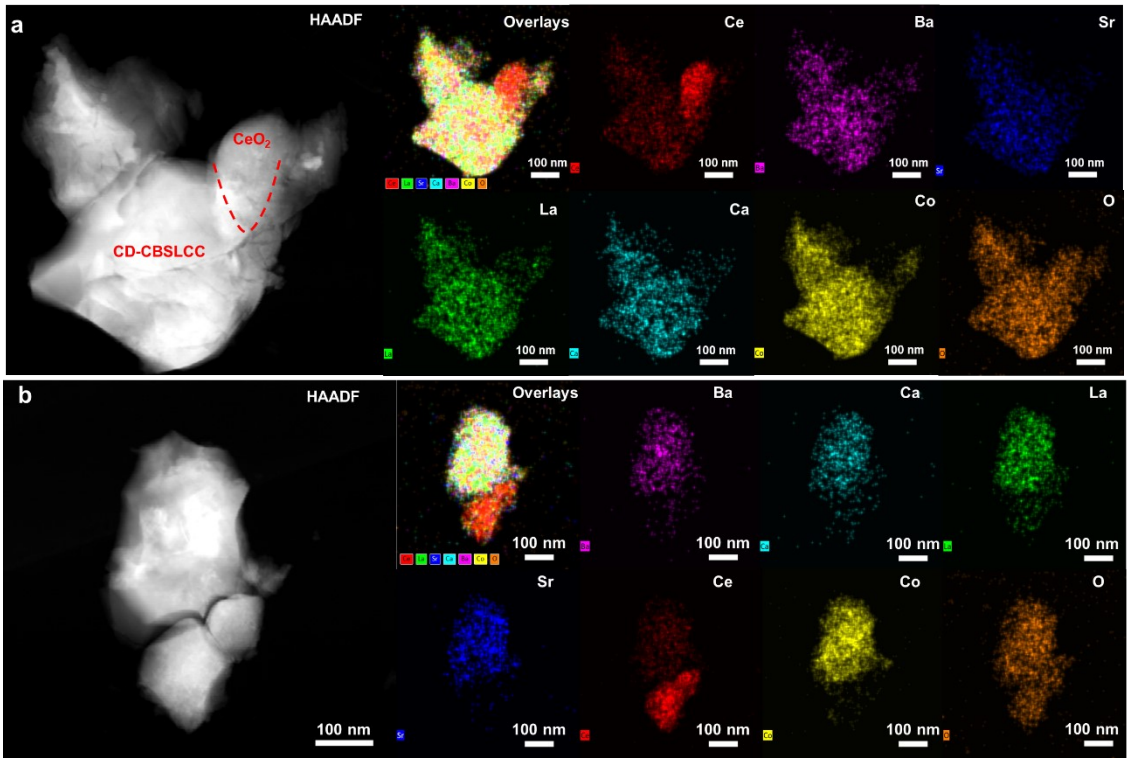

Fig. S10. (a, b) STEM-EDX result of the Ce, Ba, Sr, La, Ca, Co, and O elements from the CBSLCC grain.

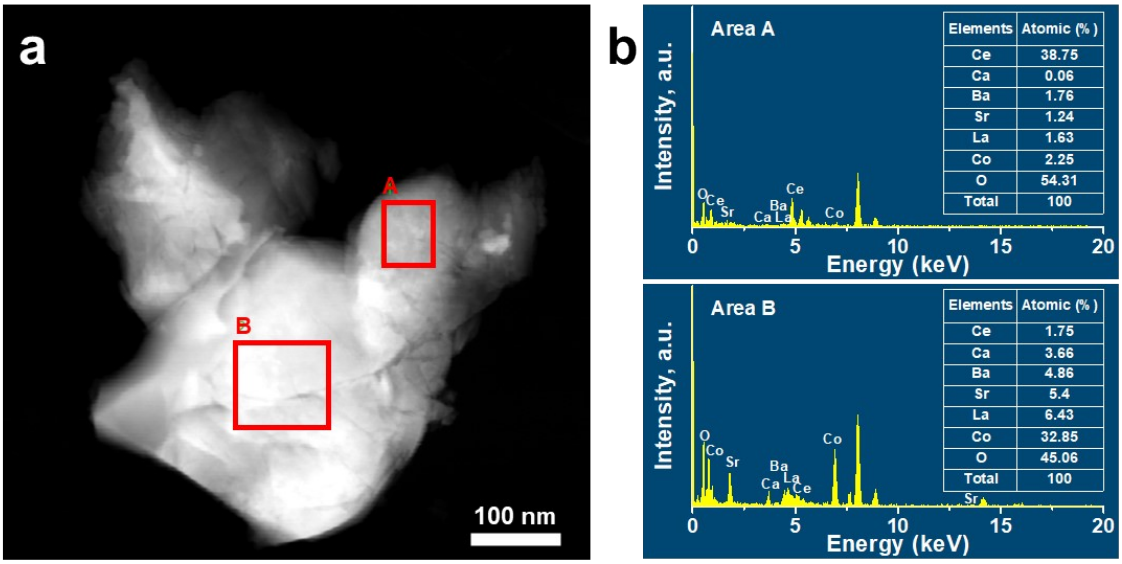

Fig. S11. (a) A STEM image of the selected CBSLCC powders. **(b)** EDX scanning results of points A and B in (a).

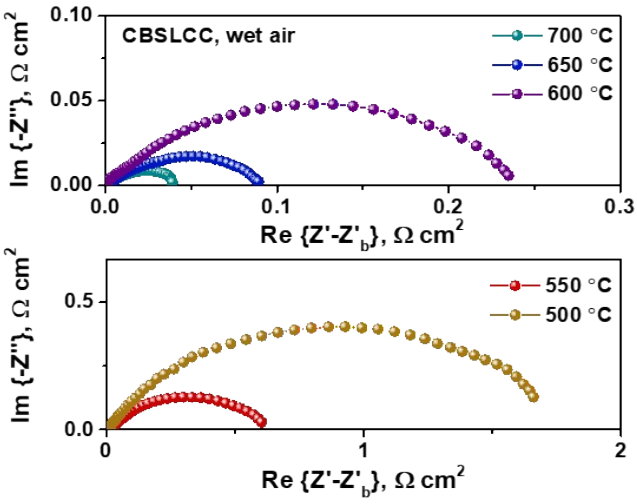

Fig. S12. Electrochemical impedance spectra (EIS) of BZCYYb-supported symmetrical cells with the CBSLCC electrode tested in wet air (3% H_2O) at 500-700 °C.

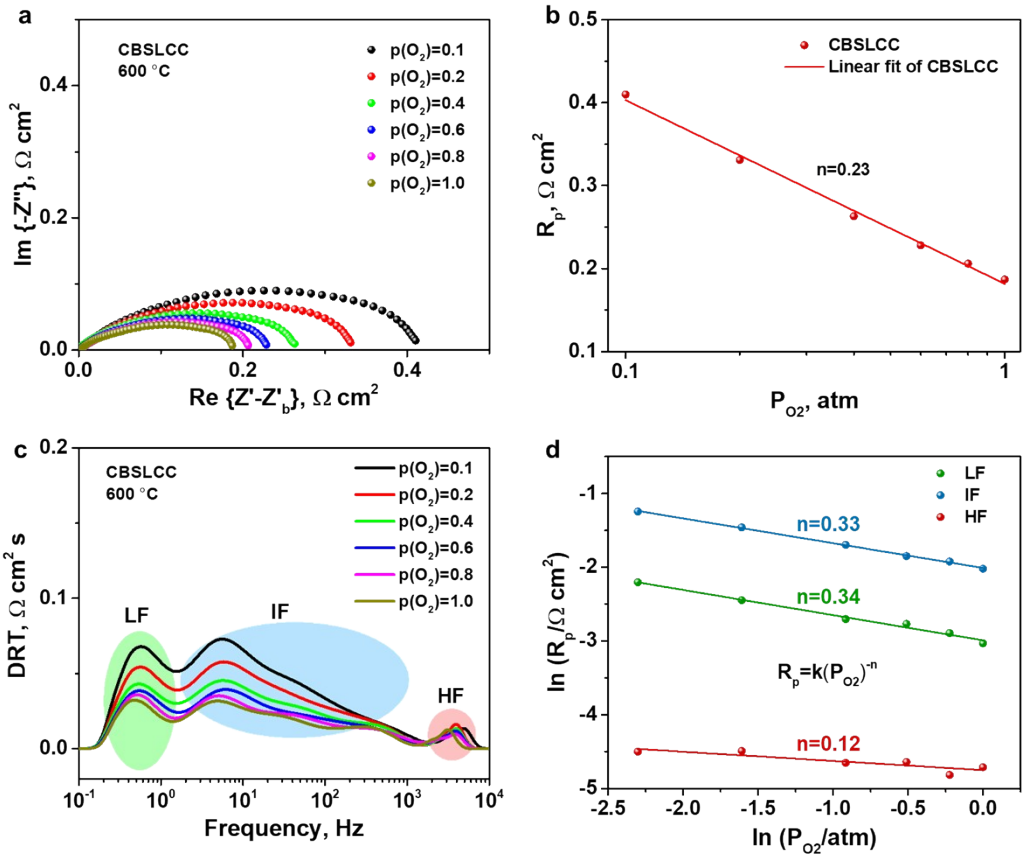

Fig. S13. (a) EIS of the symmetrical cell with the CBSLCC electrode when tested at 600 °C at different oxygen partial pressures (pO_2) of 0.1-1 atm. **(b)** Dependence of polarization resistance on pO_2 for CBSLCC at 600 °C. **(c)** DRT of the CBSLCC electrode when tested at 600 °C at different pO_2. **(d)** dependence of R_p of CBSLCC at different frequency range at 750 °C, as a function of pO_2.

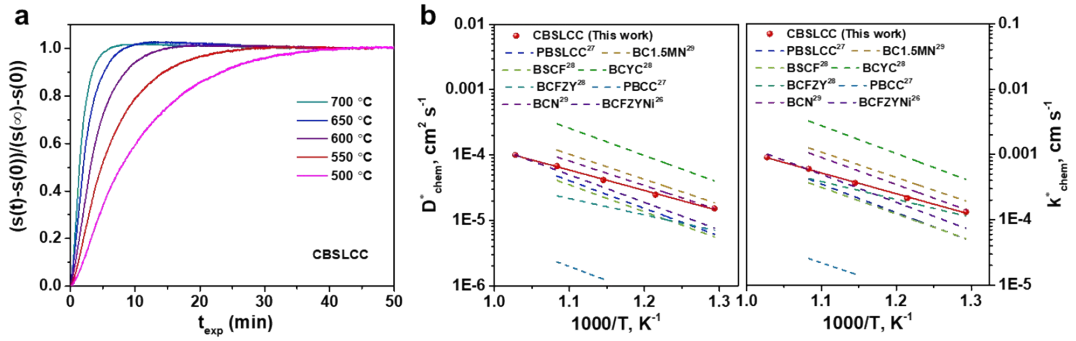

Fig. S14. (a) ECR response curves obtained for CBSLCC at 700-500 °C by suddenly changing the oxygen partial pressure of the surrounding atmosphere from 0.21 atm to 0.1 atm. **(b)** Comparison on Arrhenius plots of oxygen tracer diffusivity (D^*_{chem}) (left) and surface oxygen exchange coefficient (k^*_{chem}) (right) with other reported cathode oxides, such as $Pr_{0.2}Ba_{0.2}Sr_{0.2}La_{0.2}Ca_{0.2}CoO_{3-\delta}$ (PBSLCC), $Ba_2Co_{1.5}Mo_{0.25}Nb_{0.25}O_{6-\delta}$ (BC1.5MN), $Ba_{0.5}Sr_{0.5}Co_{0.8}Fe_{0.2}O_{3-\delta}$ (BSCF), $BaCo_{0.4}Fe_{0.4}Zr_{0.1}Y_{0.1}O_{3-\delta}$ (BCFZY), $BaCo_{0.7}Ce_{0.24}Y_{0.06}O_{3-\delta}$ (BCYC), $PrBa_{0.8}Ca_{0.2}Co_2O_{6-\delta}$ (PBCC), $BaCo_{0.75}Nb_{0.25}O_{3-\delta}$ (BCN), $Ba_{0.95}(Co_{0.4}Fe_{0.4}Zr_{0.1}Y_{0.1})_{0.95}Ni_{0.05}O_{3-\delta}$ (BCFZYNi).[26-29]

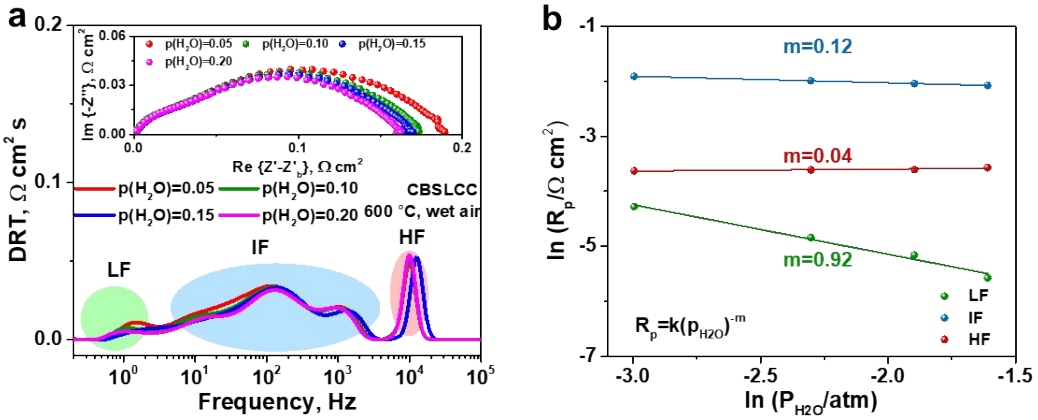

Fig. S15. (a) DRT of the CBSLCC electrode as a function of $p(H_2O)$ measured at 600 °C, inset is the corresponding EIS of the CBSLCC electrode. **(d)** Dependence of each R_p at IF, LF, and HF ranges as a function of $p(H_2O)$.

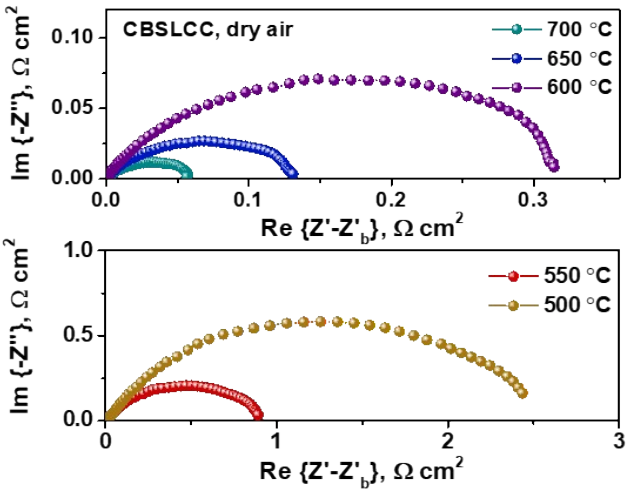

Fig. S16. EIS of BZCYYb-supported symmetrical cells with the CBSLCC electrode tested in dry air at 500-700 °C.

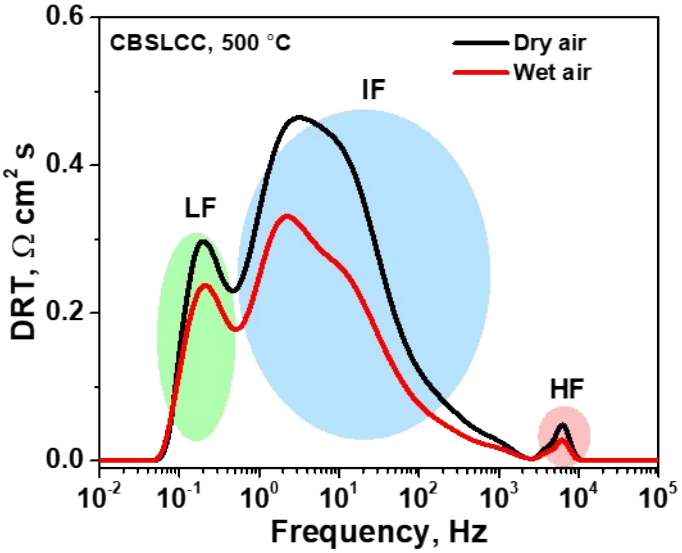

Fig. S17. DRT analysis of the CBSLCC electrode measured in dry and wet air at 500 °C.

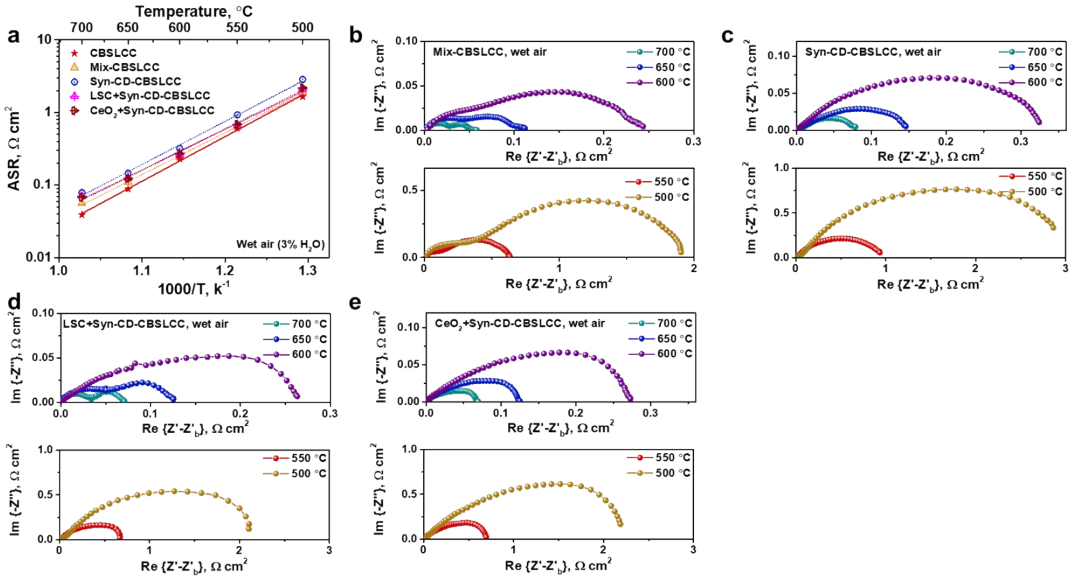

Fig. S18. **(a)** Arrhenius plot of polarization resistance (R_p) for the symmetrical cells with the CBSLCC composite, Syn-CD-CBSLCC, LSC+Syn-CD-CBSLCC, CeO_2+Syn-CD-CBSLCC and physically mixed CBSLCC (denote as Mix-CBSLCC, and its composition is 81.7 wt % Syn-CD-CBSLCC, 15.2 wt% CeO_2 and 2.9 wt% LSC) electrodes at 500-700 °C; EIS of the cells with the **(b)** Mix-CBSLCC, **(c)** Syn-CD-CBSLCC, **(d)** LSC+Syn-CD-CBSLCC and **(e)** CeO_2+Syn-CD-CBSLCC electrodes in wet air (3% H_2O), respectively.

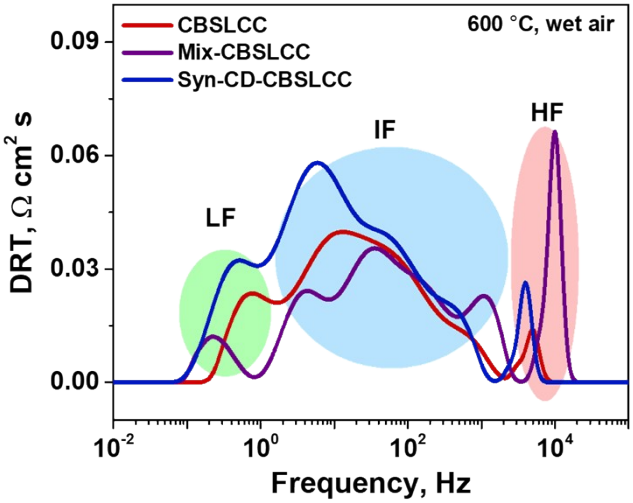

Fig. S19. DRT analysis of the CBSLCC composite, Syn-CD-CBSLCC and Mix-CBSLCC tested at 600 °C in wet air (3% H_2O).

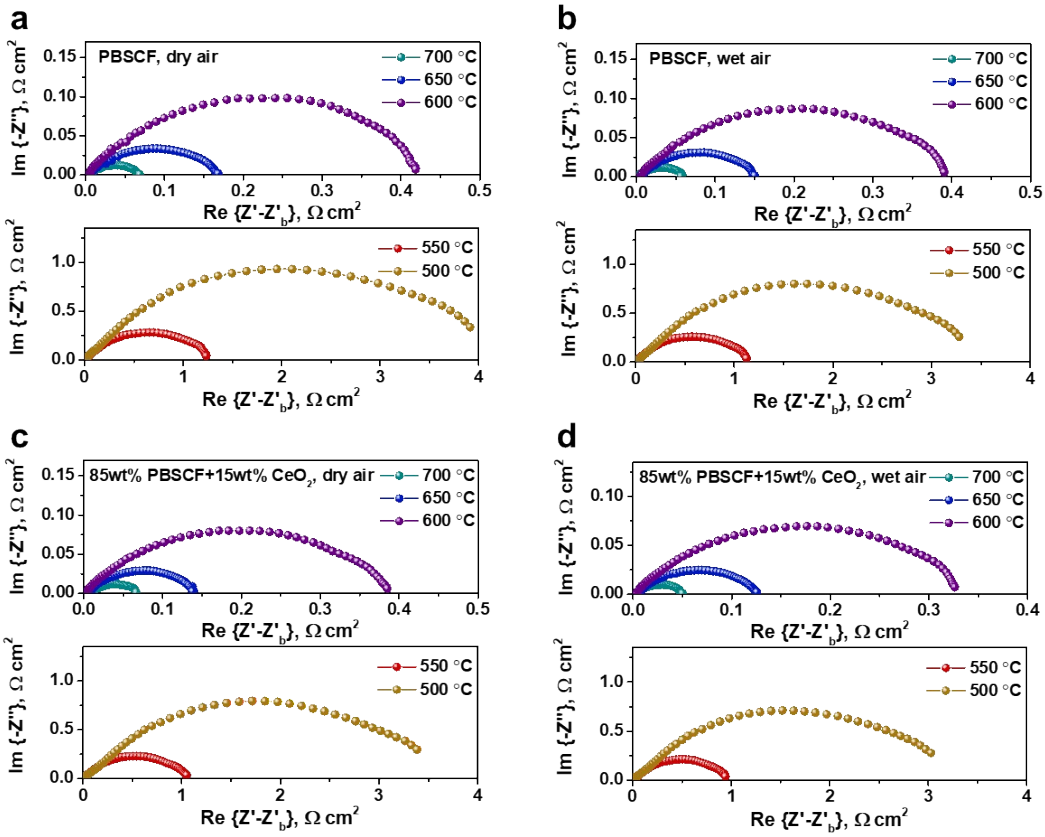

Fig. S20. EIS of BZCYYb-supported symmetrical cells with the PBSCF electrode tested at 500-700 °C in **(a)** dry air and **(b)** wet air (3% H_2O). EIS of BZCYYb-supported symmetrical cells with the 85 wt% PBSCF-15 wt% CeO_2 electrode tested at 500-700 °C in **(c)** dry air and **(d)** wet air (3% H_2O).

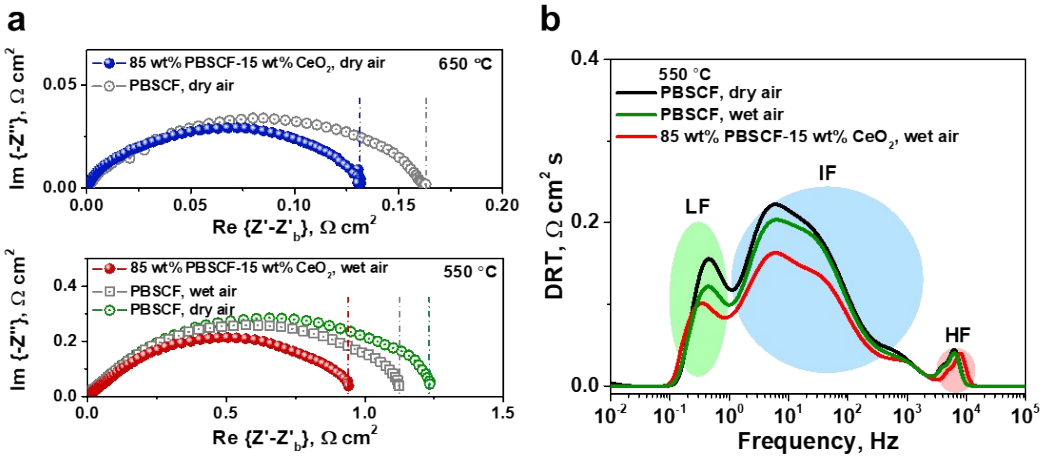

Fig. S21. (a) EIS of PBSCF and 85 wt% PBSCF-15 wt% CeO_2 electrodes measured in dry air at 650 °C (top); EIS of PBSCF and 85 wt% PBSCF-15 wt% CeO_2 electrodes measured in wet air (3% H_2O) at 550 °C (bottom), and the comparison of EIS of PBSCF tested in air at 550 °C was also added. **(b)** DRT analysis on the corresponding EIS in (a, bottom).

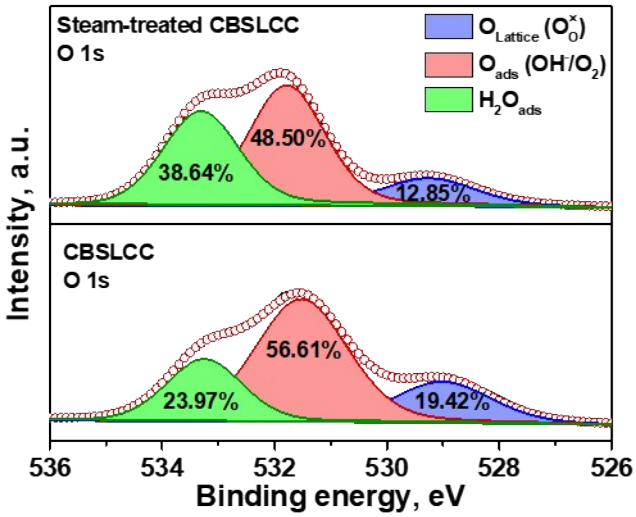

Fig. S22. Fitted O 1s XPS curves of CBSLCC composite before and after treatment in wet air (30% H_2O) at 650 °C for 50 h.

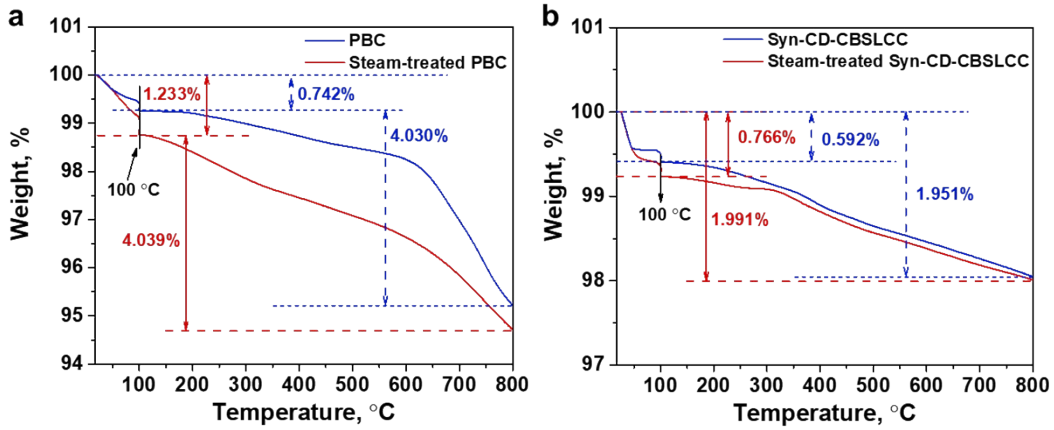

Fig. S23. (a) TGA curves of the PBC and **(b)** Syn-CD-CBSLCC samples before and after the treatments in wet air (30% H_2O) at 650 °C for 50 h at the temperature ranges of room temperature to 800 °C.

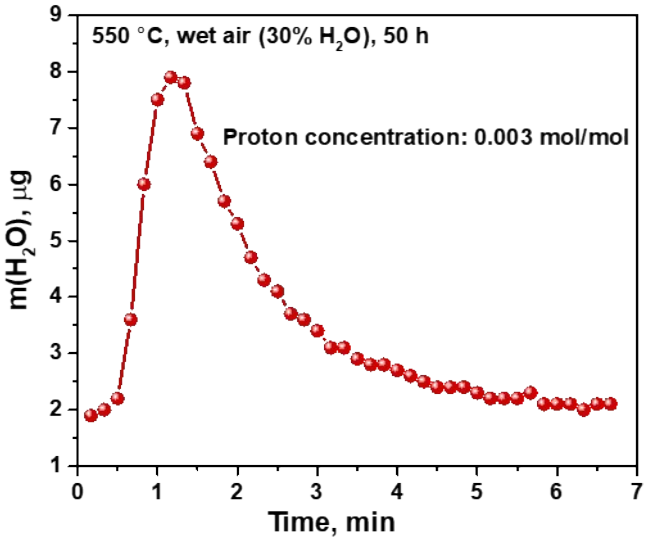

Fig. S24. The desorbed water content of the CBSLCC composite after the treatment in wet air (30% H_2O) at 550 °C for 50 h.

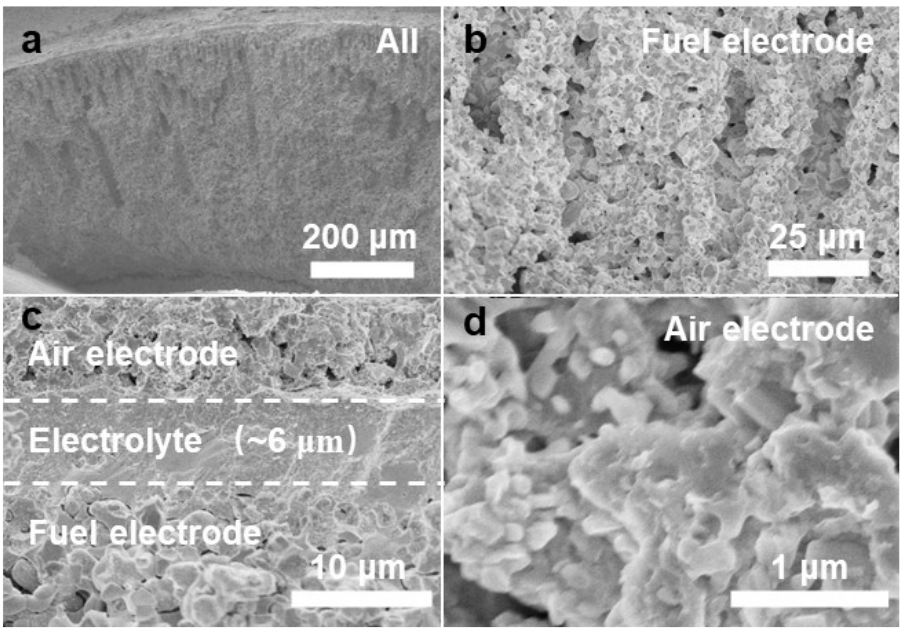

Fig. S25. Typical cross-sectional SEM images of a Ni-BZCYYb-electrode-supported tubular single cell after electrochemical tests: **(a)** an overall cross-section of the tubular cell; an enlarged view of the **(b)** fuel electrode, **(c)** the cell with air electrode, electrolyte and fuel electrode, and **(d)** air electrode.

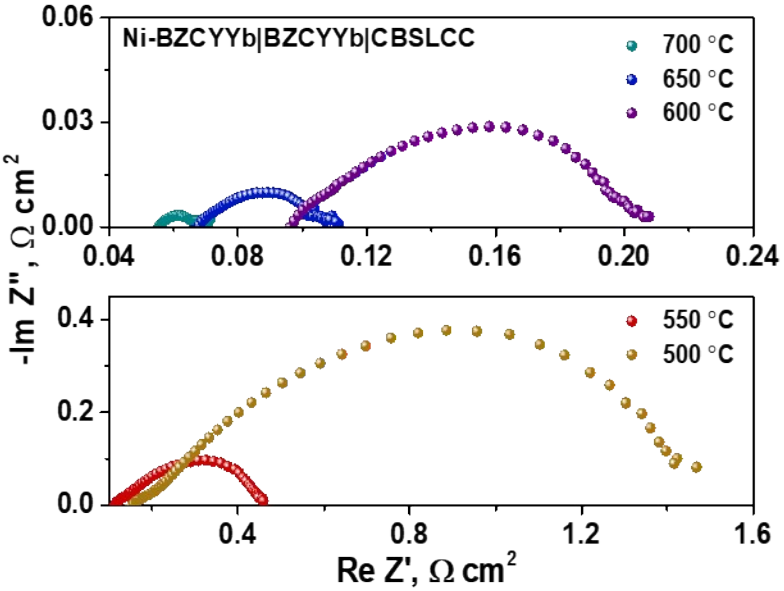

Fig. S26. EIS of a single cell with a CBSLCC electrode measured at 500-700 °C

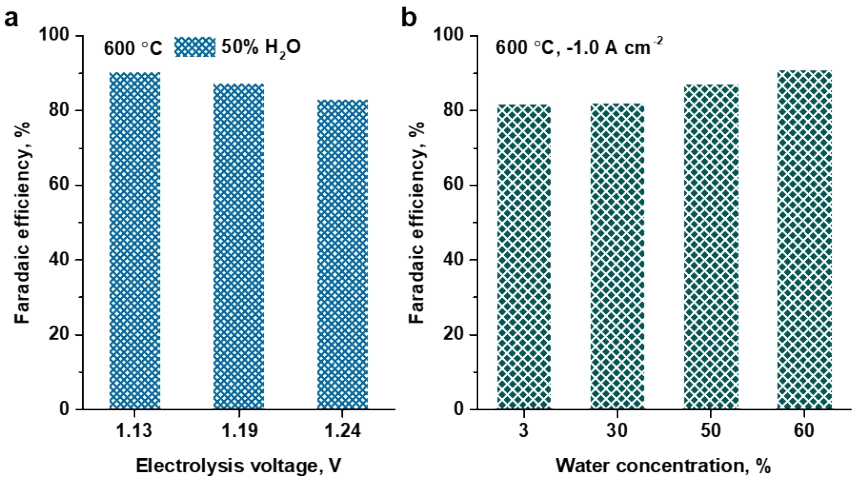

Fig. S27. (a) Faradaic efficiencies of reversible PCECs for hydrogen production at different electrolysis voltages, and **(b)** different H_2O concentrations of 3%, 30%, 50%, and 60% at 600 °C.

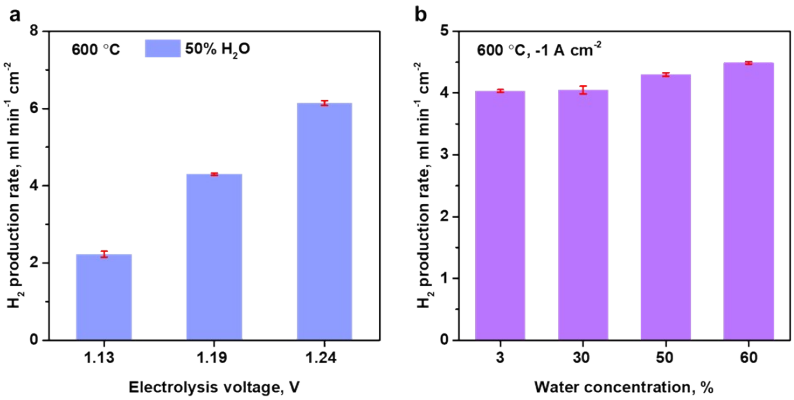

Fig. S28. (a) H_2 production rates of R-PCECs for hydrogen production at different electrolysis voltages, and **(b)** different H_2O concentrations of 3%, 20%, 30%, 50%, and 60% at 600 °C.

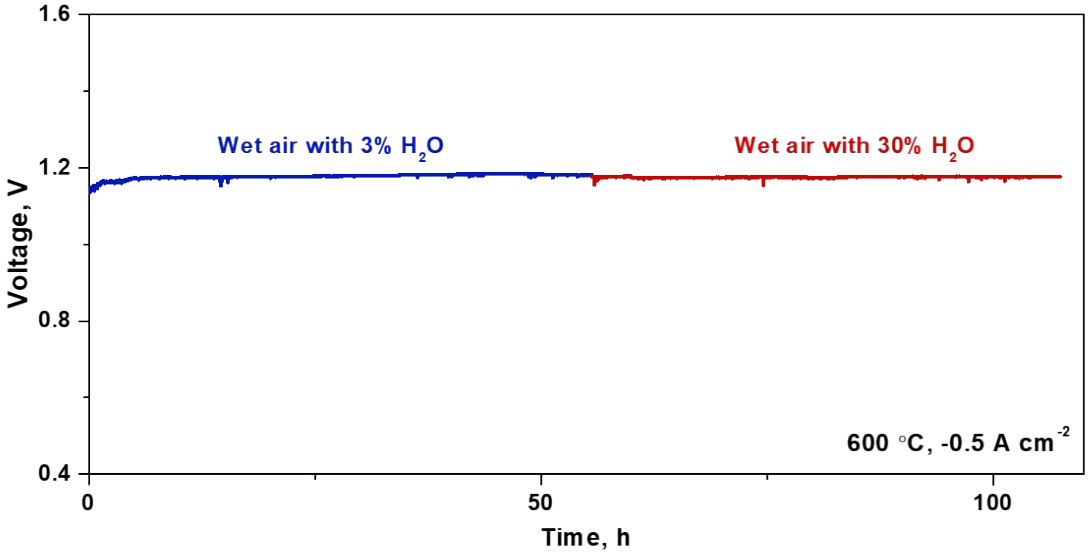

Fig. S29. Short-term stability of the R-PCEC at -0.5 A cm^{-2} when H_2O concentration was increased from 3% to 30% at 600 °C.

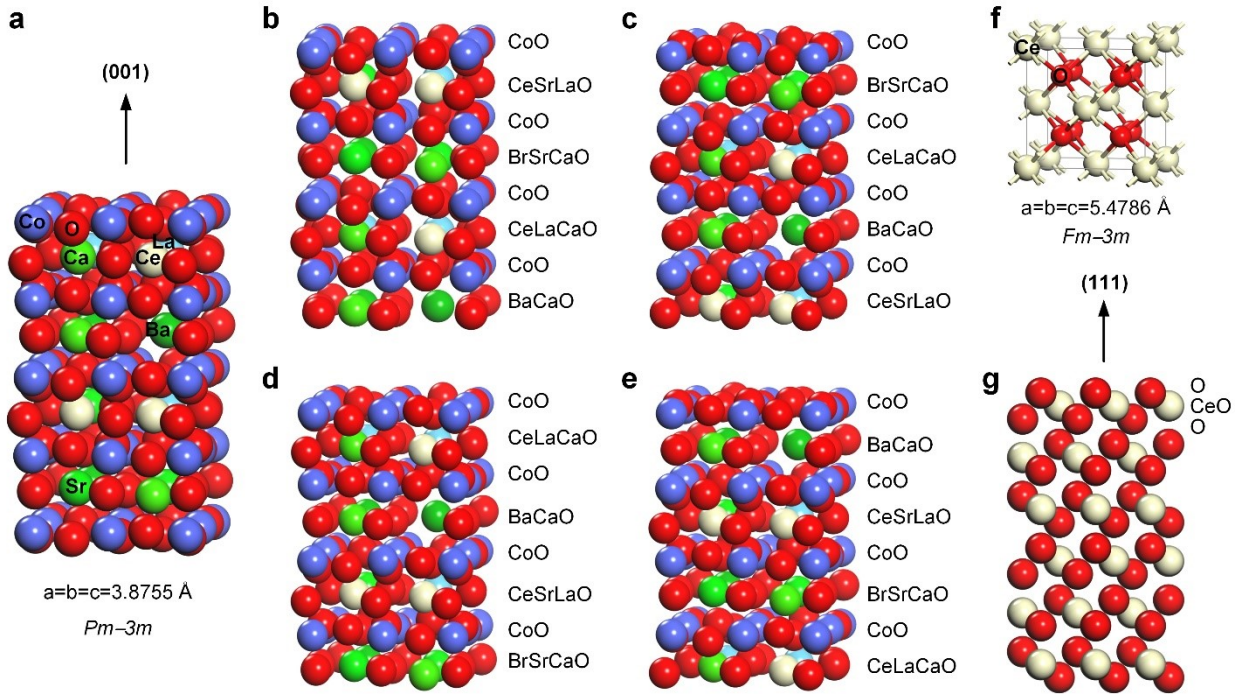

Fig. S30. (a) The bulk structure of $(Ce_{0.1875}Ba_{0.1875}Sr_{0.1875}La_{0.1875}Ca_{0.1875})CoO_3$ (CBSLCC, $Pm\bar{3}m$) and (b)-(e) eight-layer CoO-terminated CBSLCC(001) surfaces calculated using PBE + U ($U_{eff,\,Ce}$ = 5.0 eV and $U_{eff,\,Co}$ = 4.0 eV). (f) The bulk structure of CeO_2 ($Fm\bar{3}m$) and (g) the six-trilayer CeO_2(111) surface calculated using PBE + U ($U_{eff,\,Ce}$ = 5.0 eV). Note: The bulk and surface models of CBSLCC and CeO_2 do not include oxygen vacancies. Also, the Ce deficiency was implemented by removing the Ce atom from the CeLaCaO layer (**Fig. S30b**) after optimization calculations (CD-CBSLCC, $(Ce_{0.125}Ba_{0.1875}Sr_{0.1875}La_{0.1875}Ca_{0.1875})CoO_3$).

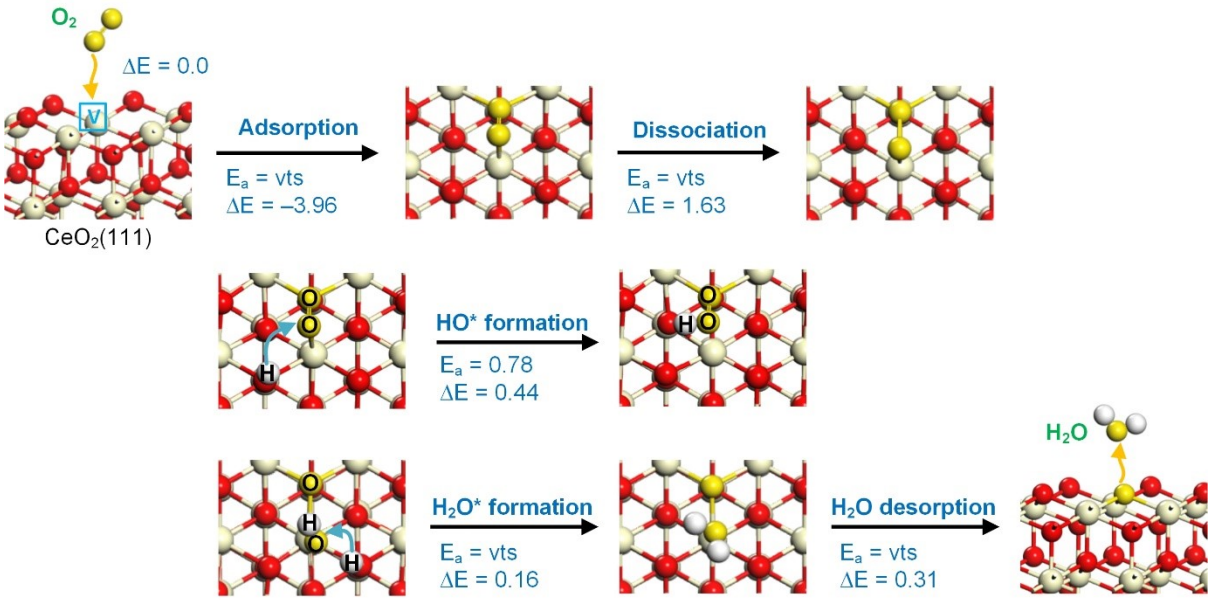

Figure S31. Reaction sequence for oxygen reduction and water formation on defective $CeO_2(111)$. Energy is in eV. "V" and "vts" represent an oxygen vacancy on the surface and an elementary process without a well-defined reaction barrier. The surface model has one oxygen vacancy on the top layer.

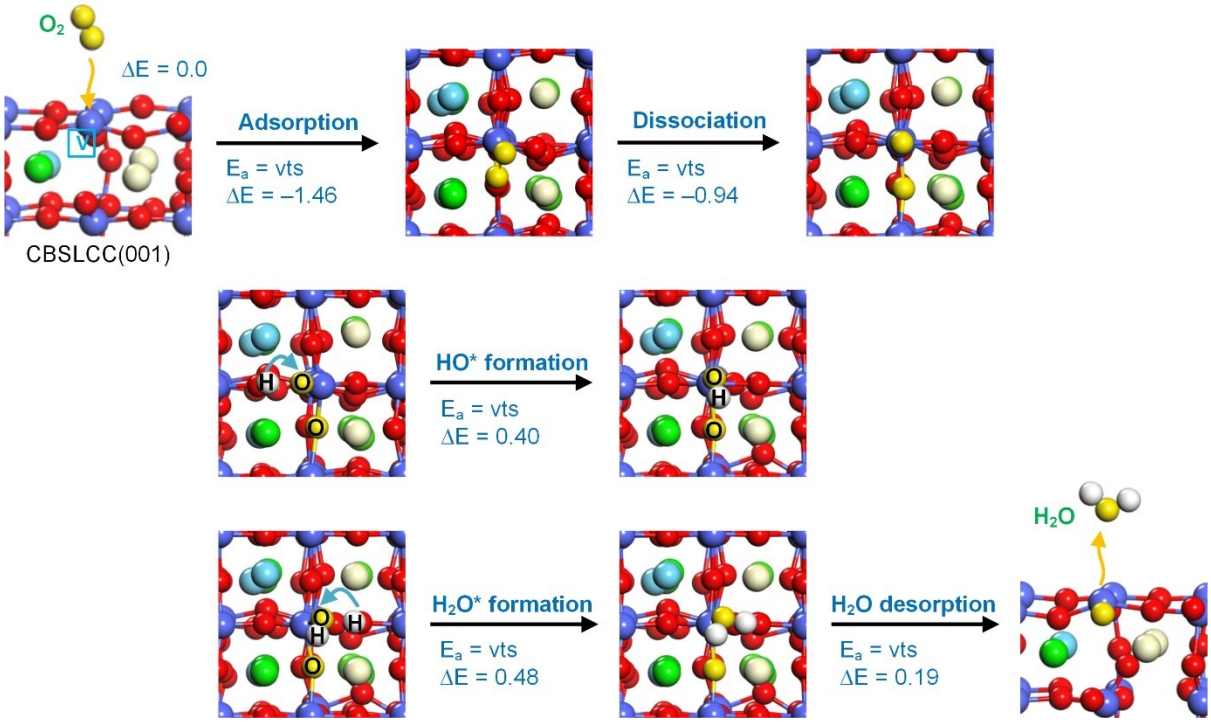

Figure S32. Reaction sequence for oxygen reduction and water formation on defective CBSLCC(001). "V" and "vts" represent an oxygen vacancy on the surface and an elementary process without a well-defined reaction barrier. The surface model has six oxygen vacancies, including one on the top layer.

Supplementary Table 1. The atomic ratio of each element in as-synthesized CBSLCC and Syn-CD-CBSLCC, measured by inductively coupled plasma mass spectrometry (ICP-MS).

Samples	Ce	Ba	Sr	La	Ca	Co
CBSLCC	0.197	0.197	0.201	0.204	0.201	1.010
Syn-CD-CBSLCC	0.047	0.256	0.218	0.223	0.256	0.990

Supplementary Table 2. Refinement parameters of CBSLCC composite sintered at 950 °C for 10 h in air.

Element	Label	x	y	z	Occupancy
Phase 1 (CD-CBSLCC, Pm**Error!**m, a=b=c=3.8492(6) Å, 81.9 wt.%)					
Ce	Ce1	0.5	0.5	0.5	0.052
Ba	Ba1	0.5	0.5	0.5	0.242
Sr	Sr1	0.5	0.5	0.5	0.232
La	La1	0.5	0.5	0.5	0.232
Ca	Ca1	0.5	0.5	0.5	0.242
Co	Co1	0	0	0	1
O	O1	0.5	0	0	1
Phase 2 (CeO_2, Fm**Error!**m, a=b=c=5.4229(6) Å, 15.2 wt.%)					
Ce	Ce1	0	0	0	1
O	O1	0.25	0.25	0.25	0.975
Phase 3 (LSC, I4/mmm, a=b=3.8454(4) Å, c=12.6102(4) Å, 2.9 wt.%)					
La	La1	0	0	0.361	0.5
Sr	Sr1	0	0	0.361	0.5
Co	Co1	0	0	0	1
O	O1	0	0.5	0	1
O	O2	0	0	0.163	1

Supplementary Table 3. The structural parameters of samples derived from R-space fitting curves of EXAFS on Ce L-edge.

Samples	Bond type	CN	R (Å)	$\sigma^2(10^{-3}Å^2)$	R factor
CBSLCC	Ce-O	10.3	2.51	8.3	0.047
Syn-CD-CBSLCC	Ce-O	11.9	2.61	11.1	0.003

*R is the distance between the absorber-scatterer pair, CN is the coordination number, σ^2 is the Debye-Waller (disorder factor), and R factor is a measure of the goodness of fit.

Supplementary Table 4. Peak fitting results of XPS spectra of the Ce 3d core level.

Sample	CBSLCC			Steam-treated CBSLCC		
Peak	Position/eV	Area	Ce^{3+}/ Ce^{4+}	Position/eV	Area	Ce^{3+}/ Ce^{4+}
$1Ce^{4+}$	882.23	10480.01		882.23	5033.03	
$2Ce^{3+}$	886.20	7173.35		886.20	3283.21	
$3Ce^{4+}$	889.05	10760.03		889.05	4662.84	
$4Ce^{4+}$	897.83	10495.59	18.7/81.3	897.83	4760.62	18.5/81.5
$5Ce^{4+}$	900.80	6986.68		900.80	3355.35	
$6Ce^{3+}$	904.70	4782.24		904.70	2188.81	
$7Ce^{4+}$	907.40	7173.35		907.40	3108.56	
$8Ce^{4+}$	915.88	6266.53		916.18	3173.75	

Supplementary Table 5. Temperature dependence of the polarization resistance (R_p) of BZCYYb symmetrical cells with CBSLCC and other high-performance electrodes reported recently.

Cathode	Temp. [°C]	R_p [Ω cm^{-2}]	Authors, Year
$Ce_{0.2}Ba_{0.2}Sr_{0.2}La_{0.2}Ca_{0.2}CoO_{3-\delta}$ (CBSLCC)	700	0.039	**This work**
	650	0.088	
	600	0.23	
	550	0.6	
	500	1.65	
$PrBa_{0.5}Sr_{0.5}Co_{1.5}Fe_{0.5}O_{6-\delta}$ (PBSCF)	700	0.057	**This work**
	650	0.147	
	600	0.39	
	550	1.123	
	500	3.5	
$Ba_2Co_{1.5}Mo_{0.25}Nb_{0.25}O_{6-\delta}$ (BC1.5MN)	700	0.07501	He, F., *et al, 2022*[29]
	650	0.13494	
	600	0.23885	
	550	0.47993	
	500	1.09348	
$Ba_{0.5}Sr_{0.5}Co_{0.8}Fe_{0.2}O_{3-\delta}$ (BSCF)	650	0.1	Song, Y., *et al, 2018*[28]
	600	0.2	
	550	0.38	
	500	0.75	
$La_{0.6}Sr_{0.4}Co_{0.2}Fe_{0.8}O_{3-\delta}$ (LSCF)	700	0.09	Zhou, Y., *et al., 2021*[51]
	650	0.18	
	600	0.51	
	550	1.05	
	500	1.29	
$BaCo_{0.4}Fe_{0.4}Zr_{0.1}Y_{0.1}O_{3-\delta}$ (BCFZY)	700	0.10	Matsui, T., *et al., 2021*[52]
	650	0.40	

	600	0.85	
	550	1.15	
$BaCo_{0.7}Ce_{0.24}Y_{0.06}O_{3-\delta}$ (BCYC)	650	0.08	Song, Y.*, et al., 2019*[28]
	600	0.25	
	550	0.49	
	500	1.39	
$PrBa_{0.8}Ca_{0.2}Co_2O_{6-\delta}$ (PBCC)	700	0.06	Zhou, Y., *et al., 2020*[53]
	650	0.102	
	600	0.3	
	550	0.6	
	500	1.5	
$PrBa_{0.8}Sr_{0.2}Co_2O_{6-\delta}$ (PBSC)	700	0.08	He, F., *et al, 2023*[27]
	650	0.15	
	600	0.35	
	550	0.95	
	500	2.5	
$Pr_{0.2}Ba_{0.2}Sr_{0.2}La_{0.2}Ca_{0.2}CoO_{3-\delta}$ (PBSLCC)	700	0.061	He, F., *et al, 2023*[27]
	650	0.12	
	600	0.26	
	550	0.75	
	500	2.13	

Supplementary Table 6. Performance comparison of our cell with the CBLSCC air electrode and other high-performance single cells reported recently.

Air electrode	Electrolyte	Fuel electrode	Electrolyte thickness [μm]	Temp. [°C]	P_{max} [W cm^{-2}]	Authors, Year
$Ce_{0.2}Ba_{0.2}Sr_{0.2}La_{0.2}Ca_{0.2}CoO_{3-\delta}$ (CBSLCC)	$BaZr_{0.1}Ce_{0.7}Y_{0.1}Yb_{0.1}O_{3-\delta}$ (BZCYYb1711)	NiO-BZCYYb1711	6	700 650 600 550	2.77 2.15 1.66 1.14	**This work**
$BaCo_{0.7}(Ce_{0.8}Y_{0.2})_{0.3}O_{3-\delta}$ (BCCY)	BZCYYb1711	NiO-BZCYYb1711	16.1	650 600 550 500 450	0.99 0.74 0.51 0.32 0.19	Song et al., 2019[28]
$PrNi_{0.5}Co_{0.5}O_{3-\delta}$ (PNC) in 70% O_2-30% H_2O	BZCYYb1711	NiO-BZCYYb1711	22	600 550 500 450	1.7 1.25 0.9 0.64	Bian et al., 2022[37]
$Gd_{0.3}Ca_{2.7}Co_{3.82}Cu_{0.18}O_{9-\delta}$ (GCCC)-BZCYYb1711	BZCYYb1711	NiO-BZCYYb1711	~10	700 650 600 550 500 450	2.05 1.6 1.16 0.77 0.48 0.28	Saqib et al., 2021[47]
$La_{0.6}Sr_{0.4}Co_{0.2}Fe_{0.8}O_{3-\delta}$ (LSCF)-BZCYYb1711	BZCYYb1711	NiO-BZCYYb1711	14	700 650 600 550	1.06 0.81 0.59 0.39	Shimada et al., 2021[38]

				500	0.25	
$NdBa_{0.5}Sr_{0.5}Co_{1.5}Fe_{0.5}O_{5+\delta}$ (NBSCF)	BZCYYb1711	NiO-BZCYYb1711	14.7	700 650 600	1.37 1.06 0.69	Kim et al., 2014[39]
$PrBa_{0.5}Sr_{0.5}Co_{1.5}Fe_{0.5}O_{5+\delta}$（PBSCF）	BZCYYb1711	NiO-BZCYYb1711	5	650 600 550 500	1.9 1.48 1.01 0.7	Choi et al., 2021[40]
$BaCe_{0.6}Zr_{0.3}Y_{0.2}O_{3-\delta}$ (BZCY632)-$BaCo_{0.4}Fe_{0.4}Zr_{0.1}Y_{0.1}O_{3-\delta}$ (BCFZY)	$BaZr_{0.4}Ce_{0.4}Y_{0.1}Yb_{0.1}O_{3-\delta}$+1 wt% NiO (BZCYYb4411)	NiO-BZCYYb4411	15	650 600	0.65 0.52	Duan et al., 2015[41]
$PrBa_{0.5}Sr_{0.5}Co_{1.5}Fe_{0.5}O_{5+\delta}$（PBSCF）	BZCYYb1711	NiO-BZCYYb1711	14.1	700 650 600	1.37 1.05 0.70	Seong et al., 2018[42]
$La_{0.6}Sr_{0.4}CoO_{3-\delta}$ (LSC)	$BaCe_{0.55}Zr_{0.3}Y_{0.15}O_{3-\delta}$ (BCZY)	NiO-BCZY, NiO-YSZ	1	650 600 550	1.3 1.1 0.8	Bae et al., 2018[43]
$Ba_{0.75}La_{0.125}FeO_{3-\delta}$ (BLF)	BZCYYb1711	NiO-BZCYYb1711	4	700 650 600 550 500	2.05 1.6 1.3 0.91 0.6	Wang et al., 2022[44]
$PrBa_{0.5}Sr_{0.5}Co_{1.5}Fe_{0.5}O_{5+\delta}$（PBSCF）	BZCYYb1711	NiO-BZCYYb1711	10	700 650 600 550	1.61 1.26 0.72 0.36	Zhang et al., 2021[45]
$Ba_{0.9}Co_{0.7}Fe_{0.2}Nb_{0.1}O_{3-\delta}$ (BCFN)	BZCYYb1711	NiO-BZCYYb1711	10	650	1.71	Pei et al., 2022[46]

				600 550 500	1.21 0.82 0.55	
$Pr_{0.2}Ba_{0.2}Sr_{0.2}La_{0.2}Ca_{0.2}CoO_{3-\delta}$ (PBSLCC)	BZCYYb1711	NiO-BZCYYb1711	10	650 600 550 500	1.51 1.16 0.72 0.4	He et al., 2022[27]
$Ba_{0.95}Ag_{0.05}Co_{0.4}Fe_{0.4}Zr_{0.1}Y_{0.1}O_{3-\delta}$ (BAgCFZY)	BZCYYb1711	NiO-BZCYYb1711	10	600 550 500 450	0.76 0.57 0.4 0.25	Kim et al., 2022[48]
$PrNi_{0.5}Co_{0.5}O_{3-\delta}$ (PNC) nano-fiber	BZCYYb1711	NiO-BZCYYb1711	10	600 550 500 450	0.62 0.44 0.3 0.18	Ding et al., 2020[54]

Supplementary Table 7. Electrolysis performance comparison of our cell and other cells reported by others.

Air electrode	Electrolyte	Fuel electrode	Electrolyte thickness [μm]	Temp. [°C]	Current Density@1.3V [A cm^{-2}]	Authors, Year
$Ce_{0.2}Ba_{0.2}Sr_{0.2}La_{0.2}Ca_{0.2}CoO_{3-\delta}$ (CBSLCC)	BZCYYb1711	NiO-BZCYYb1711	6	700 650 600 550	3.87 2.95 1.76 0.84	**This work**
$Ba_2Co_{1.5}Mo_{0.25}Nb_{0.25}O_{6-\delta}$ (BC1.5MN)	$BaZr_{0.1}Ce_{0.7}Y_{0.1}Yb_{0.1}O_{3-\delta}$ (BZCYYb1711)	NiO-BZCYYb1711	10	650 600 550	-2.05 -1.37 -0.68	He et al., 2022[29]
$NdBa_{0.5}Sr_{0.5}Co_{1.5}Fe_{0.5}O_{5+\delta}$ (NBSCF)-BZCYYb1711	BZCYYb1711	NiO-BZCYYb1711	14.7	650 600 550	-1.705 -0.805 -0.399	Kim et al., 2018[55]
$PrBa_{0.5}Sr_{0.5}Co_{1.5}Fe_{0.5}O_{5+\delta}$（PBSCF）	$BaZr_{0.8}Y_{0.2}O_{3-\delta}$ (BZY)	NiO-BZY	15	600 550 500	-0.903 -0.708 -0.5	Duan et al., 2019[56]
$PrBa_{0.5}Sr_{0.5}Co_{1.5}Fe_{0.5}O_{5+\delta}$（PBSCF）	$BaHf_{0.3}Ce_{0.5}Y_{0.1}Yb_{0.1}O_{3-\delta}$ (BHCYYb)	NiO-BHCYYb	15	650 600	-0.695 -0.285	Murphy et al., 2020[57]
Pr_2NiO_4-$BaZr_{0.2}Ce_{0.6}Y_{0.2}O_{3-\delta}$ (BZCY)	BZCY	NiO-BZCY	20	650 600 550	-0.604 -0.349 -0.221	Li et al., 2018[58]
$Pr_{1/6}La_{1/6}Nd_{1/6}Ba_{1/6}Sr_{1/6}Ca_{1/6}CoO_{3-\delta}$ (PLNBSCC)	BZCYYb1711	NiO-BZCYYb1711	6.5	600 550 500	-1.5 -1.2 -0.8	Liu et al. 2022[59]
$Gd_{0.3}Ca_{2.7}Co_{3.82}Cu_{0.18}$	BZCYYb1711	NiO-BZCYYb1711	~10	700	-4.15	Saqib et al., 2021[47]

$O_{9-\delta}$ (GCCC)-BZCYYb1711				650 600 550 500	-3.2 -2.2 -1.3 -0.8	
$La_{1.2}Sr_{0.8}NiO_4$	$BaCe_{0.68}Zr_{0.1}Y_{0.1}Yb_{0.1}Cu_{0.02}O_{3-\delta}$ (BCZYYbCu)	NiO-BCZYYbCu	13	700 650 600	-1.96 -1.21 -0.59	Yang et al. 2018[60]
$PrCo_{0.5}Ni_{0.5}O_{3-\delta}$ nano-fiber	BZCYYb4411	NiO-BZCYYb4411	~10	600 550	-1.000 -0.698	Ding et al., 2019[34]
$Pr_{0.2}Ba_{0.2}Sr_{0.2}La_{0.2}Ca_{0.2}CoO_{3-\delta}$ (PBSLCC)	BZCYYb1711	NiO-BZCYYb1711	10	650 600 550 500	2.68 1.75 0.8 0.28	He et al., 2023[27]
$PrNi_{0.5}Co_{0.5}O_{3-\delta}$ (PNC) in 70% O_2-30% H_2O	BZCYYb1711	NiO-BZCYYb1711	22	600 550 500	2.4 1.5 1.1	Bian et al., 2022[37]

Supplementary Table 8. Calculated cohesive energies per atom, bulk oxygen vacancy formation energies (E_{vac}), and O *p*-band center of bulk CBSLCC and CD-CBSLCC.

Model	Cohesive energy (eV/atom)	E_{vac} (eV)[1]	O *p*-band center (eV)[2]	Remark
CBSLCC	–3.46	1.26 (1.01)	–1.86	perfect structure
CD-CBSLCC	–3.31	0.92 (0.91)	–1.56	Ce-deficient structure

[1] Oxygen vacancies were calculated using the bulk models of CBSLCC (3 Ce, 3 Ba, 3 Sr, 3 La, 3 Ca, 16 Co, 48 O atoms) and Ce-deficient CBSLCC (CD-CBSLCC, 2 Ce, 3 Ba, 3 Sr, 3 La, 3 Ca, 16 Co, 48 O atoms) with only the Γ point to reduce the computational times, and they were averaged. Those in parentheses were calculated by removing the four lowest oxygen vacancies computed using only the Γ point with a Γ-centered (4 × 4 × 2) ***k***-point grid.

[2] The O 2-*p* band centers were calculated using PBE + U up to the filled orbitals with a (3 × 3 × 3) ***k***-point grid.

Supplementary Table 9. Surface energies (E_{surf}) of CoO-terminated perfect and defective CBSLCC(001) surfaces.

Surface	Termination[1]	CBSLCC(001)	CD-CBSLCC(001)
I	CoO-CeSrLaO	0.57	0.59[2]
II	CoO-BaSrCaO	1.33	1.33
III	CoO-CeLaCaO	0.99	0.87
IV	CoO-BaCaO	1.34	0.80

[1] The configurations are shown in **Figure S30**.

[2] This termination was used for the mechanistic studies after generating six oxygen vacancies for CD-CBSLCC.

References

1. F. He, Q. Gao, Z. Liu, M. Yang, R. Ran, G. Yang, W. Wang, W. Zhou and Z. Shao, *Advanced Energy Materials*, 2021, **11**, 2003916.
2. Y. Pan, H. Zhang, K. Xu, Y. Zhou, B. Zhao, W. Yuan, K. Sasaki, Y. Choi, Y. Chen and M. Liu, *Applied Catalysis B: Environmental*, 2022, **306**, 121071.
3. B. Ravel and M. Newville, *Journal of synchrotron radiation*, 2005, **12**, 537-541.
4. G. Kresse and J. Hafner, *Physical Review B*, 1993, **47**, 558-561.
5. G. Kresse and J. Furthmuller, *Physical Review B*, 1996, **54**, 11169-11186.
6. J. P. Perdew, K. Burke and M. Ernzerhof, *Physical Review Letters*, 1996, **77**, 3865-3868.
7. P. E. Blöchl, *Physical Review B*, 1994, **50**, 17953-17979.
8. M. Nolan, S. Grigoleit, D. C. Sayle, S. C. Parker and G. W. Watson, *Surface Science*, 2005, **576**, 217-229.
9. A. M. Ritzmann, J. M. Dieterich and E. A. Carter, *Physical Chemistry Chemical Physics*, 2016, **18**, 12260-12269.
10. Y.-L. Lee, J. Kleis, J. Rossmeisl, Y. Shao-Horn and D. Morgan, *Energy & Environmental Science*, 2011, **4**, 3966-3970.
11. R. Jacobs, J. Hwang, Y. Shao-Horn and D. Morgan, *Chemistry of Materials*, 2019, **31**, 785-797.
12. B. M. Bokstein, M. I.; Srolovitz, D. J., *Thermodynamics and Kinetics in Materials Science: A Short Course*, Oxford Univ. Press, New York, 2005.
13. D. A. Dimitrakis, N. I. Tsongidis and A. G. Konstandopoulos, *Physical Chemistry Chemical Physics*, 2016, **18**, 23587-23595.
14. H. Ding, A. V. Virkar, M. Liu and F. Liu, *Physical Chemistry Chemical Physics*, 2013, **15**, 489-496.
15. Y. Choi, M. Scott, T. Söhnel and H. Idriss, *Physical Chemistry Chemical Physics*, 2014, **16**, 22588-22599.
16. R. Zhai, C. Deng, S. Du and L. Li, *Chemical Physics*, 2023, **564**, 111708.
17. Z. Yang, T. K. Woo, M. Baudin and K. Hermansson, *Journal of Chemical*

Physics, 2004, **120**, 7741-7749.

18. G. Henkelman, B. P. Uberuaga and H. Jónsson, *Journal of Chemical Physics*, 2000, **113**, 9901-9904.
19. L. Shen, Z. Du, Y. Zhang, X. Dong and H. Zhao, *Applied Catalysis B: Environmental*, 2021, **295**, 120264.
20. S. Zhai, H. Xie, P. Cui, D. Guan, J. Wang, S. Zhao, B. Chen, Y. Song, Z. Shao and M. Ni, *Nature Energy*, 2022, **7**, 866-875.
21. F. He, D. Song, R. Peng, G. Meng and S. Yang, *Journal of Power Sources*, 2010, **195**, 3359-3364.
22. F. He, T. Wu, R. Peng and C. Xia, *Journal of Power Sources*, 2009, **194**, 263-268.
23. F. Ciucci and C. Chen, *Electrochimica Acta*, 2015, **167**, 439-454.
24. L. Shen, Z. Du, Y. Zhang, X. Dong and H. Zhao, *Applied Catalysis B: Environmental*, 2021, **295**, 120264.
25. Z. Wang, W. Yang, S. P. Shafi, L. Bi, Z. Wang, R. Peng, C. Xia, W. Liu and Y. Lu, *Journal of Materials Chemistry A*, 2015, **3**, 8405-8412.
26. M. Liang, Y. Zhu, Y. Song, D. Guan, Z. Luo, G. Yang, S. P. Jiang, W. Zhou, R. Ran and Z. Shao, *Advanced Materials*, 2022, **34**, 2106379.
27. F. He, Y. Zhou, T. Hu, Y. Xu, M. Hou, F. Zhu, D. Liu, H. Zhang, K. Xu and M. Liu, *Advanced Materials*, 2023, 2209469.
28. Y. Song, Y. Chen, W. Wang, C. Zhou, Y. Zhong, G. Yang, W. Zhou, M. Liu and Z. Shao, *Joule*, 2019, **3**, 2842-2853.
29. F. He, S. Liu, T. Wu, M. Yang, W. Li, G. Yang, F. Zhu, H. Zhang, K. Pei and Y. Chen, *Advanced Functional Materials*, 2022, 2206756.
30. J. H. Yu, J. S. Lee and J. Maier, *Angewandte Chemie International Edition*, 2007, **46**, 8992-8994.
31. D. Poetzsch, R. Merkle and J. Maier, *Advanced Functional Materials*, 2015, **25**, 1542-1557.
32. S. Choi, C. J. Kucharczyk, Y. Liang, X. Zhang, I. Takeuchi, H.-I. Ji and S. M. Haile, *Nature Energy*, 2018, **3**, 202-210.

33. K. Kreuer, *Solid State Ionics*, 1999, **125**, 285-302.
34. H. Ding, W. Wu, C. Jiang, Y. Ding, W. Bian, B. Hu, P. Singh, C. J. Orme, L. Wang and Y. Zhang, *Nature communications*, 2020, **11**, 1-11.
35. Y. Song, J. Liu, Y. Wang, D. Guan, A. Seong, M. Liang, M. J. Robson, X. Xiong, Z. Zhang and G. Kim, *Advanced Energy Materials*, 2021, **11**, 2101899.
36. L. Yang, S. Wang, K. Blinn, M. Liu, Z. Liu, Z. Cheng and M. Liu, *Science*, 2009, **326**, 126-129.
37. W. Bian, W. Wu, B. Wang, W. Tang, M. Zhou, C. Jin, H. Ding, W. Fan, Y. Dong and J. Li, *Nature*, 2022, **604**, 479-485.
38. H. Shimada, Y. Yamaguchi, H. Sumi and Y. Mizutani, *Ceramics International*, 2021, **47**, 16358-16362.
39. J. Kim, S. Sengodan, G. Kwon, D. Ding, J. Shin, M. Liu and G. Kim, *ChemSusChem*, 2014, **7**, 2811-2815.
40. M. Choi, J. Paik, D. Kim, D. Woo, J. Lee, S. J. Kim, J. Lee and W. Lee, *Energy & Environmental Science*, 2021, **14**, 6476-6483.
41. C. Duan, J. Tong, M. Shang, S. Nikodemski, M. Sanders, S. Ricote, A. Almansoori and R. O'Hayre, *Science*, 2015, **349**, 1321-1326.
42. A. Seong, J. Kim, J. Kim, S. Kim, S. Sengodan, J. Shin and G. Kim, *Journal of The Electrochemical Society*, 2018, **165**, F1098.
43. K. Bae, D. H. Kim, H. J. Choi, J. W. Son and J. H. Shim, *Advanced Energy Materials*, 2018, **8**, 1801315.
44. Z. Wang, Y. Wang, J. Wang, Y. Song, M. J. Robson, A. Seong, M. Yang, Z. Zhang, A. Belotti, J. Liu, G. Kim, J. Lim, Z. Shao and F. Ciucci, *Nature Catalysis*, 2022, **5**, 777-787.
45. H. Zhang, Y. Zhou, K. Pei, Y. Pan, K. Xu, Y. Ding, B. Zhao, K. Sasaki, Y. Choi and Y. Chen, *Energy & Environmental Science*, 2022, **15**, 287-295.
46. K. Pei, Y. Zhou, K. Xu, H. Zhang, Y. Ding, B. Zhao, W. Yuan, K. Sasaki, Y. Choi and Y. Chen, *Nature communications*, 2022, **13**, 1-10.
47. M. Saqib, I.-G. Choi, H. Bae, K. Park, J.-S. Shin, Y.-D. Kim, J.-I. Lee, M. Jo, Y.-C. Kim and K.-S. Lee, *Energy & Environmental Science*, 2021, **14**, 2472-

2484.

48. J. H. Kim, J. Hong, D. K. Lim, S. Ahn, J. Kim, J. K. Kim, D. Oh, S. Jeon, S. J. Song and W. Jung, *Energy & Environmental Science*, 2022, **15**.

49. C. C. Duan, R. Kee, H. Y. Zhu, N. Sullivan, L. Z. Zhu, L. Z. Bian, D. Jennings and R. O'Hayre, *Nature Energy*, 2019, **4**, 230-240.

50. F. He, F. Zhu, D. Liu, Y. Zhou, K. Sasaki, Y. Choi, M. Liu and Y. Chen, *Materials Today*, 2023, **63**, 89-98.

51. Y. Zhou, W. Zhang, N. Kane, Z. Luo, K. Pei, K. Sasaki, Y. Choi, Y. Chen, D. Ding and M. Liu, *Advanced Functional Materials*, 2021, **31**, 2105386.

52. T. Matsui, N. Kunimoto, K. Manriki, K. Miyazaki, N. Kamiuchi, H. Muroyama and K. Eguchi, *Journal of Materials Chemistry A*, 2021, **9**, 15199-15206.

53. Y. Zhou, E. Liu, Y. Chen, Y. Liu, L. Zhang, W. Zhang, Z. Luo, N. Kane, B. Zhao, L. Soule, Y. Niu, Y. Ding, H. Ding, D. Ding and M. Liu, *ACS Energy Letters*, 2021, **6**, 1511-1520.

54. H. Ding, W. Wu, C. Jiang, Y. Ding, W. Bian, B. Hu, P. Singh, C. J. Orme, L. Wang, Y. Zhang and D. Ding, *Nature Communications*, 2020, **11**, 1907.

55. J. Kim, A. Jun, O. Gwon, S. Yoo, M. Liu, J. Shin, T.-H. Lim and G. Kim, *Nano Energy*, 2018, **44**, 121-126.

56. C. Duan, R. Kee, H. Zhu, N. Sullivan, L. Zhu, L. Bian, D. Jennings and R. O'Hayre, *Nature Energy*, 2019, **4**, 230-240.

57. R. Murphy, Y. Zhou, L. Zhang, L. Soule, W. Zhang, Y. Chen and M. Liu, *Advanced Functional Materials*, 2020, **30**, 2002265.

58. W. Li, B. Guan, L. Ma, S. Hu, N. Zhang and X. Liu, *Journal of Materials Chemistry A*, 2018, **6**, 18057-18066.

59. Z. Liu, Z. Tang, Y. Song, G. Yang, W. Qian, M. Yang, Y. Zhu, R. Ran, W. Wang and W. Zhou, *Nano-Micro Letters*, 2022, **14**, 217.

60. S. Yang, S. Zhang, C. Sun, X. Ye and Z. Wen, *ACS Applied Materials & Interfaces*, 2018, **10**, 42387-42396.